J. Fluid Mech. (2023), *vol*. 963, A31, doi:10.1017/jfm.2023.316

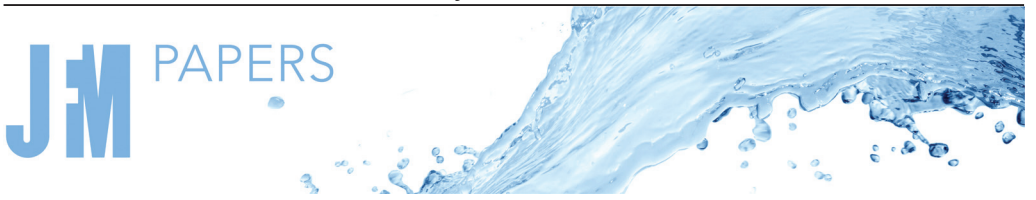

The response of small-scale shear layers to perturbations in turbulence

Tomoaki Watanabe[1],† **and Koji Nagata**[2,3]

[1]Education and Research Center for Flight Engineering, Nagoya University, Furo-cho, Chikusa, Nagoya 464-8603, Japan

[2]Department of Aerospace Engineering, Nagoya University, Furo-cho, Chikusa, Nagoya 464-8603, Japan

[3]Department of Mechanical Engineering and Science, Kyoto University, Kyoto 615-8540, Japan

(Received 21 October 2022; revised 24 February 2023; accepted 11 April 2023)

The perturbation response of small-scale shear layers in turbulence is investigated with direct numerical simulations (DNS). The analysis of shear layers in isotropic turbulence suggests that the typical layer thickness is about four times the Kolmogorov scale η. Response for sinusoidal perturbations is investigated for an isolated shear layer, which models a mean flow around the shear layers in turbulence. The vortex formation in the shear layer is optimally promoted by the perturbation whose wavelength divided by the layer thickness is about 7. These results indicate that the small-scale shear instability in turbulence is efficiently promoted by velocity fluctuations with a wavelength of about 30η. Furthermore, DNS are carried out for decaying turbulence initialised by the artificially modified velocity field of isotropic turbulence. The vortex formation from shear layers is accelerated under the influence of external perturbations with the efficient wavelength to promote the instability. When velocity fluctuations with this wavelength are eliminated by a band-cut filter, the shear layers tend to persist for a long time without producing vortices. These behaviours affect the number of vortices in turbulence, which increases and decreases when velocity perturbations with the unstable wavelength of the instability are artificially amplified and damped, respectively. The increase in the number of vortices results in the enhancement of kinetic energy dissipation, enstrophy production and strain self-amplification. These results indicate that the perturbation response of shear layers is important in the small-scale dynamics of turbulence as well as the modulation of small-scale turbulent motions by external disturbance.

Key words: shear layers, shear-flow instability

† Email address for correspondence: watanabe.tomoaki@c.nagoya-u.jp

1. Introduction

Turbulent flows are characterised by fluid motions with a wide range of length scales. Large-scale turbulent motions possess a large part of kinetic energy, which is transferred to small scales by inertial processes and eventually dissipated by viscous effects (Kolmogorov 1941; Pope 2000; Davidson 2004). The scale dependence of turbulence has been studied extensively in previous studies. The characteristics of large-scale turbulent motions depend strongly on the process by which turbulence is generated. On the other hand, small-scale motions are considered to have universal statistical properties which hardly depend on flows (Monin & Yaglom 1975; Sreenivasan & Antonia 1997). Turbulence is also studied in terms of flow structures, which are often identified as coherent patterns in flow visualisation. As also found for the statistical properties, large-scale structures are flow-dependent whereas small-scale structures are more universal (Brown & Roshko 1974; Yule 1978; Jiménez *et al.* 1993; da Silva, Dos Reis & Pereira 2011; Philip & Marusic 2012).

Small-scale properties of turbulence are often studied with a velocity gradient tensor $\boldsymbol{\nabla u}$, whose component is denoted by $\partial u_i/\partial x_j$. Hereafter, a component of vectors and matrices is denoted by subscripts, e.g. $(\boldsymbol{\nabla u})_{ij} = \partial u_i/\partial x_j$. The decomposition of $\boldsymbol{\nabla u}$ into symmetric and antisymmetric parts as $(\boldsymbol{\nabla u})_{ij} = S_{ij} + \Omega_{ij}$ is widely used to study incompressible turbulence, where $S_{ij} = (\partial u_i/\partial x_j + \partial u_j/\partial x_i)/2$ is the rate-of-strain tensor and $\Omega_{ij} = (\partial u_i/\partial x_j - \partial u_j/\partial x_i)/2$ is the rate-of-rotation tensor. One of the most famous small-scale structures in turbulence is a vortex tube with rotating motion. The radius of vortices is about four to six times the Kolmogorov scale in various turbulent flows (Jiménez *et al.* 1993; Jiménez & Wray 1998; Kida & Miura 1998; Tanahashi, Iwase & Miyauchi 2001; Kang, Tanahashi & Miyauchi 2007; Mouri, Hori & Kawashima 2007; Ganapathisubramani, Lakshminarasimhan & Clemens 2008; da Silva *et al.* 2011; Jahanbakhshi, Vaghefi & Madnia 2015; Ghira, Elsinga & da Silva 2022). Another small-scale structure observed in turbulence is a vortex sheet. The vortex sheet is a thin layer with intense shear. Therefore, the vortex sheets are also called shear layers in recent studies because the structures are identified with shear intensity or shear vorticity (Eisma *et al.* 2015; Nagata *et al.* 2020). The small-scale shear layers were originally identified in turbulence as regions with moderately large enstrophy $\omega^2/2 = \Omega_{ij}\Omega_{ij}$ when the enstrophy field was visualised to detect vortical structures (Jiménez *et al.* 1993). Because of a strong correlation between vorticity and strain in shear layers, they are also identified with an eigenvalue of the second-order velocity gradient tensor $A_{ij} = S_{ik}\Omega_{kj} + S_{jk}\Omega_{ki}$ (Horiuti & Takagi 2005). The eigenvalue of A_{ij} is useful in identifying the location of shear layers and is used to investigate the flow statistics in the regions occupied by the shear layers, which are shown to be dynamically important structures related to the budget of turbulent kinetic energy and enstrophy (Buxton & Ganapathisubramani 2010; Pirozzoli, Bernardini & Grasso 2010; Nakamura, Watanabe & Nagata 2023).

Both vortex tubes and shear layers are perceivable in an enstrophy profile because both motions of rigid-body rotation and shear contribute to a vorticity vector $\boldsymbol{\omega} = \boldsymbol{\nabla} \times \boldsymbol{u}$. Recent studies of vortex identification schemes have developed new decompositions of $\boldsymbol{\nabla u}$ by which the contribution of shearing motion is extracted from $\boldsymbol{\nabla u}$ or $\boldsymbol{\omega}$. Such examples are the triple decomposition and the Rortex-based decomposition (Kolář 2007; Liu *et al.* 2018). To distinguish vortex tubes and shear layers, the triple decomposition extracts a component of shearing motion, $\boldsymbol{\nabla u}_S$, from $\boldsymbol{\nabla u}$. The vorticity vector defined with the residual component $\boldsymbol{\nabla u} - \boldsymbol{\nabla u}_S$ contains only rigid-body rotation. Thus, the magnitudes of vorticity vectors defined for $\boldsymbol{\nabla u}_S$ and $\boldsymbol{\nabla u} - \boldsymbol{\nabla u}_S$ can identify shear layers and vortex tubes, respectively. The details of the triple decomposition can be found in Kolář (2007), which is briefly explained in § 2.2. The shear-layer identification in turbulent flows has

been reported with criteria based on the norm or vorticity of $\nabla \boldsymbol{u}_S$ (Eisma *et al.* 2015; Watanabe, Tanaka & Nagata 2020; Fiscaletti, Buxton & Attili 2021). Gul, Elsinga & Westerweel (2020) have compared shear layers detected with the triple decomposition and the eigenvalue of A_{ij} in a turbulent pipe flow and have found that the same flow regions with intense shear can be identified with both quantities. However, unlike the eigenvalue of A_{ij}, the components of $\nabla \boldsymbol{u}_S$ provide the information of shear orientation in addition to the location of shear layers. The mean flow field around shear layers in isotropic turbulence has been assessed in the reference frame defined with the shear orientation, which is identified with the triple decomposition (Watanabe & Nagata 2022). The shear layers in turbulence are formed in a region of biaxial strain. The shear layers are small-scale structures whose mean length scales are characterised by the Kolmogorov scale in isotropic turbulence and turbulent free shear flows (Watanabe *et al.* 2020; Fiscaletti *et al.* 2021; Hayashi, Watanabe & Nagata 2021*a*). The enstrophy production and strain self-amplification actively occur in the shear layers because of the interaction between the shear and biaxial strain (Watanabe *et al.* 2020; Hayashi *et al.* 2021*a*). Similar layer structures with intense shear have been observed between uniform momentum zones in wall-bounded shear flows (Eisma *et al.* 2015; Fan *et al.* 2019; Gul *et al.* 2020; Chen, Chung & Wan 2021). An experimental study on a turbulent boundary layer has shown that the thickness of these layers scales with the Taylor microscale (Eisma *et al.* 2015) while the thickness of small-scale shear layers found in isotropic turbulence, jets and mixing layers scales with the Kolmogorov scale. Therefore, it is not clear at this moment if the shear layers that separate the uniform momentum zones are the same as the small-scale shear layers found in turbulence far from the wall although both layer structures are characterised by intense shear.

Flow visualisation has revealed that a roll-up of small-scale shear layers results in the formation of a vortex tube by a similar process to Kelvin–Helmholtz instability (Vincent & Meneguzzi 1994; Passot *et al.* 1995; Watanabe *et al.* 2020). The dynamics of the roll-up process in a shear flow are often studied with an ideal model of a shear layer, which is initially uniform in the flow direction. These studies mostly concern large-scale shear flows, which are observed in plane mixing layers, jets and separated flows although they might be relevant to the instability of small-scale shear layers in turbulence. The instability of a parallel uniform shear flow has been studied with a linear stability theory, which relies on a linearised equation for small pertubations (Miles 1961; Betchov & Szewczyk 1963; Maslowe & Thompson 1971). Although the linear model of the shear layer is usually applied to an early stage of the layer development, the predicted initial growth rate of the instability is consistent with numerical simulations of Navier–Stokes equations (Patnaik, Sherman & Corcos 1976). Other studies also consider a parallel shear flow in a biaxial strain field, which is also known as Burgers' vortex (Lin & Corcos 1984; Beronov & Kida 1996). Both linear and nonlinear analyses of these uniform shear flows have confirmed that the growth of the instability strongly depends on the wavelength of perturbations. When the wavelength matches the most unstable mode of the instability, the perturbed shear layer rapidly develops and results in a fast roll-up. This wavelength dependence is often taken into account in numerical simulations of turbulent shear flows, which rapidly develop from a laminar state with the perturbations of the most unstable mode (Moser & Rogers 1991; Caulfield & Peltier 1994; Vreman, Geurts & Kuerten 1995; Abraham & Magi 1997; Le Ribault, Sarkar & Stanley 1999; Okong'o & Bellan 2002; Stanley, Sarkar & Mellado 2002). The dependence of the instability on the perturbation wavelength has also proved useful in flow control, by which a flow is forced by actuators or passive objects. The flow is often efficiently modulated when an external disturbance matches the frequency band of instabilities (Crow & Champagne 1971; Oster & Wygnanski 1982). The application of this flow control strategy has been reported for

various turbulent shear flows, which include canonical free shear flows and more practical flows such as a flow over an airfoil (Ghoniem & Ng 1987; Gutmark, Schadow & Yu 1995; Soteriou & Ghoniem 1995; Brehm, Gross & Fasel 2013; Samimy, Webb & Crawley 2018)

One of the interesting questions is whether small-scale shear layers in turbulence also have a wavenumber dependence in the response to perturbations, as also observed for uniform shear layers considered as numerical and analytical models and large-scale shear layers in laboratory experiments. Considering the application of the results of stability analysis in active flow control of large-scale shear flows, one may expect that the response of small-scale shear layers to perturbations will be important in the studies of modulation of turbulence. For example, small-scale perturbations can be introduced in particle-laden flows by the interaction between small particles and turbulence (Maxey 2017). As also considered for active flow control of turbulent shear flows, the perturbation response of small-scale shear layers can be important in establishing the strategy of active flow control of small-scale turbulent motions (Buzzicotti, Biferale & Toschi 2020; Cazaubiel *et al.* 2021). In addition, it can also be important in understanding the interaction of turbulent motions with different scales. The roll-up of the shear layers may be understood as the interaction between small-scale shearing motion and velocity fluctuations at larger scales. The interaction between different scales of motions is often investigated in wavenumber space (Yeung & Brasseur 1991; Ohkitani & Kida 1992; Aluie & Eyink 2009). However, some turbulent structures are difficult to identify in wavenumber space because the structures are not defined solely by their scales. For this reason, a large number of publications have been devoted to the investigation of turbulent structures in physical space. It is sometimes considered that the structural approach to turbulence is less rigorous than the statistical approach because the former mostly relies on flow visualisation and thresholds applied to flow variables. However, both approaches are important in understanding turbulence from different aspects as discussed in Tsinober (2009). For example, small-scale intermittency can be discussed with the scaling exponents for structure functions (Kholmyansky, Tsinober & Yorish 2001) while the spatiotemporal distributions of variables defined with a velocity gradient tensor often explain these statistical behaviour from the viewpoint of turbulent structures (Siggia 1981; Jiménez *et al.* 1993). The perturbation response of small-scale shear layers observed in physical space may shed light on a physical process that underlies the interaction of different scales in wavenumber space.

Most fundamental studies on shear instability assume a uniform shear layer, whose thickness is much smaller than the length scale in the other directions. However, visualisation of shear layers in turbulence has suggested that this assumption is not valid as they have a pancake or ribbon shape with a finite aspect ratio (Buxton & Ganapathisubramani 2010; Bhatt & Tsuji 2021; Fiscaletti *et al.* 2021; Hayashi *et al.* 2021*a*). For this reason, it is not clear how the stability analysis of shear flows with an infinite aspect ratio is related to the evolution of small-scale shear layers in turbulence. This might be because early studies of small-scale shear layers have relied on flow visualisation, which does not provide important parameters in the stability analysis, such as the probability distribution of thickness and velocity jump of the shear layers. However, recent studies have overcome these difficulties with the new statistical analysis of small-scale shear layers based on the conditional averaging procedure in a local reference frame defined for each shear layer (Eisma *et al.* 2015; Fiscaletti *et al.* 2021; Watanabe *et al.* 2020).

This study aims to investigate the response of small-scale shear layers in turbulence to perturbations, which may be relevant to vortex formation due to the instability in turbulence. Three kinds of numerical simulations are carried out for this purpose. First, the characteristics of shear layers are investigated with direct numerical simulations

(DNS) of statistical steady homogeneous isotropic turbulence to reveal the variations of length and velocity scales and shear Reynolds number among shear layers. The analysis of shear layers in homogeneous isotropic turbulence is presented in § 2. Based on the results for isotropic turbulence, numerical simulations for an isolated shear layer with a finite aspect ratio subject to a biaxial strain are performed in § 3 to examine the development of the perturbed shear layer. The model follows Burgers' vortex layer except for the aspect ratio and approximates a mean flow observed around the shear layers in turbulence. Furthermore, § 4 presents DNS of decaying turbulence which is initialised with an artificially modified velocity field of isotropic turbulence. The DNS is carried out to investigate the response of shear layers to external perturbations or velocity fluctuations that internally exist in turbulence. For the former case, the initial field of DNS is obtained by superimposing perturbations with a certain length scale on isotropic turbulence. The latter considers decaying turbulence initialised with a band-cut filtered velocity field of isotropic turbulence. The length scale of the perturbations and filter is determined based on the other two simulations carried out to examine the shear layer characteristics and the response of the isolated shear layer to perturbations. These simulations are compared with decaying turbulence of original isotropic turbulence to confirm whether vortex formation in turbulence can be promoted by velocity fluctuations with a wavelength within the shear instability band. Finally, the paper is summarised in § 5.

2. Characteristics of small-scale shear layers in turbulence

2.1. *DNS of statistically steady homogeneous isotropic turbulence*

DNS databases of statistically steady homogeneous isotropic turbulence are analysed to relate the small-scale shear layers in turbulence to a model of an isolated shear layer in § 3, where some parameters are determined based on the results presented in this section. The DNS databases are the same as those used in our previous studies (Watanabe *et al.* 2020; Watanabe, Tanaka & Nagata 2021; Watanabe & Nagata 2022). Turbulence is sustained at a statistically steady state with a linear forcing scheme (Carroll & Blanquart 2013) The governing equations are the Navier–Stokes equations for an incompressible fluid, which are written as

$$\frac{\partial u_j}{\partial x_j} = 0, \tag{2.1}$$

$$\frac{\partial u_i}{\partial t} + u_j \frac{\partial u_i}{\partial x_j} = -\frac{1}{\rho}\frac{\partial p}{\partial x_i} + \nu \frac{\partial^2 u_i}{\partial x_j^2} + f_i, \tag{2.2}$$

where u_i is the velocity vector, p is the pressure, ρ is the constant density, ν is the kinematic viscosity and f_i is the forcing term (Carroll & Blanquart 2013). The DNS code is based on the fractional step method and employs a fourth-order fully conservative finite-difference scheme for spatial discretisation (Morinishi *et al.* 1998) and a third-order and low-storage Runge–Kutta method for temporal advancement (Spalart, Moser & Rogers 1991). The Poisson equation for pressure is solved with the biconjugate gradient stabilised method.

Table 1 summarises the parameters of DNS databases. Here, the statistics are defined with volume averages in the computational domain and ensemble averages of different time instances. An average of a variable f is denoted by $\langle f \rangle$. The spatial resolution Δ is about 0.8 times the Kolmogorov scale $\eta = (\nu^3/\varepsilon_0)^{1/4}$, where $\varepsilon_0 = \langle 2\nu S_{ij} S_{ij} \rangle$ is the averaged kinetic energy dissipation rate. Table 1 includes the Reynolds numbers based on the integral scale and Taylor microscale, which are defined as $Re_L = u_0 L_0/\nu$ and

Case	NS1	NS2	NS3	NS4
N^3	256^3	512^3	1024^3	2048^3
Δ/η	0.83	0.82	0.84	0.82
Re_L	122	361	1092	2709
Re_λ	43	72	128	202

Table 1. Parameters of DNS of statistically steady homogeneous isotropic turbulence: the number of grid points N^3, the spatial resolution Δ/η and Reynolds numbers based on the integral scale and Taylor microscale (Re_L and Re_λ).

$Re_\lambda = u_0\lambda/\nu$, respectively. When the linear forcing scheme is used, the integral scale is often evaluated as $L_0 = u_0^3/\varepsilon_0$ with the root-mean-squared (r.m.s.) velocity fluctuations $u_0 = \sqrt{(\langle u^2\rangle + \langle v^2\rangle + \langle w^2\rangle)/3}$ because L_0 normalised by the domain size is determined as the property of the forcing scheme (Rosales & Meneveau 2005; Carroll & Blanquart 2013; Watanabe *et al.* 2021). On the other hand, the Taylor microscale is evaluated as $\lambda = \sqrt{15\nu u_0^2/\varepsilon_0}$. For the present DNS databases, Re_λ ranges from 43 to 202.

2.2. *Analysis of small-scale shear layers in turbulence*

The small-scale shear layers in isotropic turbulence are analysed by detecting the shear layers with the triple decomposition of a velocity gradient tensor, as also reported in previous studies of shear layers in turbulent flows (Eisma *et al.* 2015; Watanabe *et al.* 2020; Fiscaletti *et al.* 2021). The DNS databases are analysed with the procedures briefly described below. Previous studies can be referred to for further details of the algorithms of the triple decomposition (Kolář 2007; Nagata *et al.* 2020; Fiscaletti *et al.* 2021) and the shear layer analysis (Watanabe & Nagata 2022) .

The shear layers are detected with the triple decomposition (Kolář 2007), which considers three local fluid motions: shear, rigid-body rotation and elongation (irrotational strain). The velocity gradient tensor $\boldsymbol{\nabla u}$ is decomposed into the components associated with these motions as $\boldsymbol{\nabla u} = \boldsymbol{\nabla u}_S + \boldsymbol{\nabla u}_R + \boldsymbol{\nabla u}_E$, where the subscripts, S, R and E, represent shear, rotation and elongation, respectively. The triple decomposition has to be applied in a so-called basic reference frame, which is different depending on position and time. The basic reference frame is the reference frame where the decomposition formula can most effectively extract the shear contribution from $\boldsymbol{\nabla u}$ among all the reference frames. The basic reference frame can be specified from reference frames defined with three sequential rotational transformations $\boldsymbol{Q}(\theta_1, \theta_2, \theta_3)$ with $0^\circ \le \theta_1 \le 180^\circ$, $0^\circ \le \theta_2 \le 180^\circ$ and $0^\circ \le \theta_3 \le 90^\circ$. The rotational transformation tensor $\boldsymbol{Q}(\theta_1, \theta_2, \theta_3)$ is written as

$$\boldsymbol{Q} = \begin{pmatrix} \cos\theta_1\cos\theta_2\cos\theta_3 - \sin\theta_1\sin\theta_3 & \sin\theta_1\cos\theta_2\cos\theta_3 + \cos\theta_1\sin\theta_3 & -\sin\theta_2\cos\theta_3 \\ -\cos\theta_1\cos\theta_2\sin\theta_3 - \sin\theta_1\cos\theta_3 & -\sin\theta_1\cos\theta_2\sin\theta_3 + \cos\theta_1\cos\theta_3 & \sin\theta_2\sin\theta_3 \\ \cos\theta_1\sin\theta_2 & \sin\theta_1\sin\theta_2 & \cos\theta_2 \end{pmatrix}. \tag{2.3}$$

The velocity gradient tensor in a rotated reference frame is calculated as $(\boldsymbol{\nabla u})^* = \boldsymbol{Q}(\boldsymbol{\nabla u})\boldsymbol{Q}^T$, where $*$ represents a quantity evaluated in the rotated reference frame. The basic reference frame can be identified with a quantity called an interaction scalar, $I^* = |\Omega_{12}^* S_{12}^*| + |\Omega_{23}^* S_{23}^*| + |\Omega_{31}^* S_{31}^*|$. The basic reference frame assumes that I^* has the largest value among all reference frames defined with $\boldsymbol{Q}$ for $0^\circ \le \theta_1 \le 180^\circ$, $0^\circ \le \theta_2 \le 180^\circ$ and

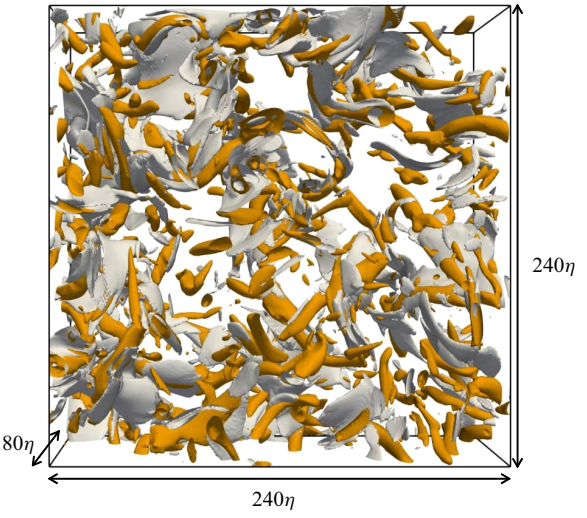

Figure 1. Visualisation of shear layers and vortices, which are identified with the isosurfaces of $I_S = 2\langle I_S\rangle$ (white) and $I_R = 4\langle I_R\rangle$ (orange), respectively (NS2). Only a small part of the computational domain is shown here.

$0^\circ \le \theta_3 \le 90^\circ$. By discretely changing the angles, I^* is calculated for many reference frames. Then, $(\theta_1, \theta_2, \theta_3)$ which gives the largest I_S^* is used to define the basic reference frame. The angles are changed by 5°, for which the basic reference frame is accurately determined (Nagata *et al.* 2020; Fiscaletti *et al.* 2021). In the basic reference frame, the following decomposition is applied to extract $(\nabla \boldsymbol{u}_S)^*$:

$$(\nabla \boldsymbol{u}_{RES})^*_{ij} = \mathrm{sgn}[(\nabla \boldsymbol{u})^*_{ij}]\,\min[|(\nabla \boldsymbol{u})^*_{ij}|, |(\nabla \boldsymbol{u})^*_{ji}|], \tag{2.4}$$

$$(\nabla \boldsymbol{u}_S)^*_{ij} = (\nabla \boldsymbol{u})^*_{ij} - (\nabla \boldsymbol{u}_{RES})^*_{ij}, \tag{2.5}$$

for $i, j = 1, 2$ and 3 and sgn is a sign function. In addition, $(\nabla \boldsymbol{u}_{RES})^*$ is further decomposed into the components of rotation and elongation as $(\nabla \boldsymbol{u}_R)^*_{ij} = [(\nabla \boldsymbol{u}_{RES})^*_{ij} - (\nabla \boldsymbol{u}_{RES})^*_{ji}]/2$ and $(\nabla \boldsymbol{u}_E)^*_{ij} = [(\nabla \boldsymbol{u}_{RES})^*_{ij} + (\nabla \boldsymbol{u}_{RES})^*_{ji}]/2$. Finally, $(\nabla \boldsymbol{u}_S)$, $(\nabla \boldsymbol{u}_R)$ and $(\nabla \boldsymbol{u}_E)$ in the original coordinate are obtained by applying the inverse transformation of $\boldsymbol{Q}$ to $(\nabla \boldsymbol{u}_S)^*$, $(\nabla \boldsymbol{u}_R)^*$ and $(\nabla \boldsymbol{u}_E)^*$. The intensities of motions of shear and rotation are defined as $I_S = \sqrt{2(\nabla \boldsymbol{u}_S)_{ij}(\nabla \boldsymbol{u}_S)_{ij}}$ and $I_R = \sqrt{2(\nabla \boldsymbol{u}_R)_{ij}(\nabla \boldsymbol{u}_R)_{ij}}$. Figure 1 visualises the isosurfaces of I_R and I_S in NS2. These quantities are often used to detect vortices and shear layers in a three-dimensional flow. The shear layers identified with I_S (white) have a flat shape whereas vortex tubes are detected with I_R (orange).

The small-scale shear layers in turbulence can be identified as flow regions with large shear intensity I_S. Therefore, following Watanabe *et al.* (2020), the present study examines a flow field around the local maxima of I_S. Here, the Hessian matrix of I_S, $\partial^2 I_S/\partial x_i \partial x_j$, uniquely determines the locations of the local maxima without thresholds (Hayashi, Watanabe & Nagata 2021*b*). For each detected local maximum, a local shear coordinate $(\zeta_1, \zeta_2, \zeta_3)$ is introduced to observe the flow in a reference frame associated with shearing motion. The velocity vector in the shear coordinate is denoted by (u_1, u_2, u_3). The shear coordinate assumes that the shear is expressed with $\partial u_3/\partial \zeta_2$. In this case, the shear contributes to the vorticity in the ζ_1 direction. Therefore, the ζ_1 direction is given by the unit vorticity vector of $\nabla \boldsymbol{u}_S$, $\boldsymbol{\omega}_S/|\boldsymbol{\omega}_S|$, where $(\boldsymbol{\omega}_S)_i = \epsilon_{ijk}(\nabla \boldsymbol{u}_S)_{jk}$ is a component of shear vorticity $\boldsymbol{\omega}_S$ and ϵ_{ijk} is the Levi-Civita symbol. Then, ζ_2 and ζ_3 are determined such that

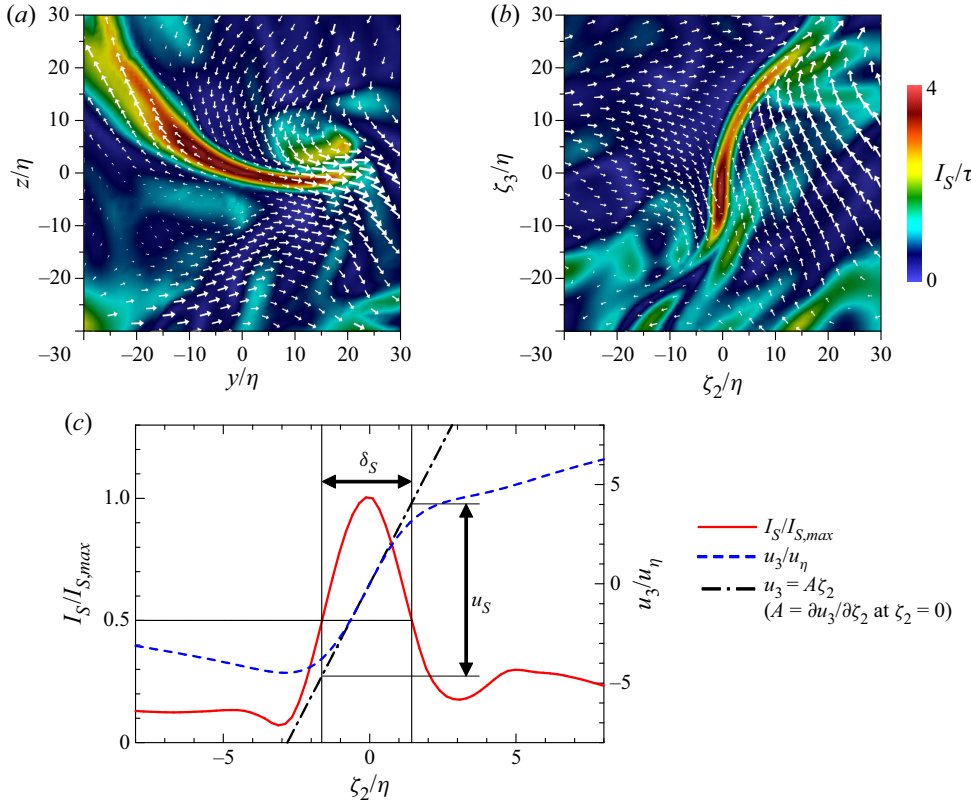

Figure 2. A local flow field around a shear layer in (*a*) the coordinate used in DNS and (*b*) the shear coordinate. The local maximum of I_S is located at the centre of each figure. A colour contour of shear intensity I_S normalised by the Kolmogorov time scale $\tau_\eta = (\nu/\varepsilon_0)^{1/2}$ and two-dimensional velocity vectors relative to the fluid motion at $(y, z) = (0, 0)$ or $(\zeta_2, \zeta_3) = (0, 0)$ are shown on the two-dimensional planes. The length of the arrows represents the vector magnitude. (*c*) Variations of I_S and velocity in the ζ_3 direction, u_3, across the shear layer visualised in (*b*) along the ζ_2 axis at $(\zeta_1, \zeta_3) = (0, 0)$.

shearing motion is expressed with $\partial u_3/\partial\zeta_2$. The identification of ζ_2 and ζ_3 is based on a similar algorithm used to identify the basic reference frame. A large number of different reference frames are examined to identify the reference frame in which $(\nabla \boldsymbol{u}_S)_{32}$ becomes the largest among all the reference frames under the condition that the ζ_1 direction is given by $\boldsymbol{\omega}_S/|\boldsymbol{\omega}_S|$. The numerical algorithm to find the shear coordinate is described in detail in Watanabe *et al.* (2020) and Hayashi *et al.* (2021*a*).

Once the shear coordinate is identified for a location of a local maximum of I_S, flow variables on the DNS grid, namely $f(x, y, z)$, are interpolated onto the shear coordinate with a third-order polynomial interpolation, providing $f(\zeta_1, \zeta_2, \zeta_3)$. Here, the shear coordinate is also discretised with a spacing smaller than the Kolmogorov scale. The interpolation on the shear coordinate is applied for all local maxima of I_S. Figure 2(*a*,*b*) visualise one of the detected shear layers in NS2 in the reference frame of DNS (x, y, z) and in the shear coordinate $(\zeta_1, \zeta_2, \zeta_3)$. The shear intensity I_S and the velocity vectors with respect to the velocity at the centre are shown on the two-dimensional planes. As the shear layers have no preference in the alignment with (x, y, z), a shear flow is not always observed in the reference frame of DNS in figure 2(*a*). The shearing motion in the shear coordinate is represented by the flows in the $\pm\zeta_3$ directions. In figure 2(*b*), these parallel flows in

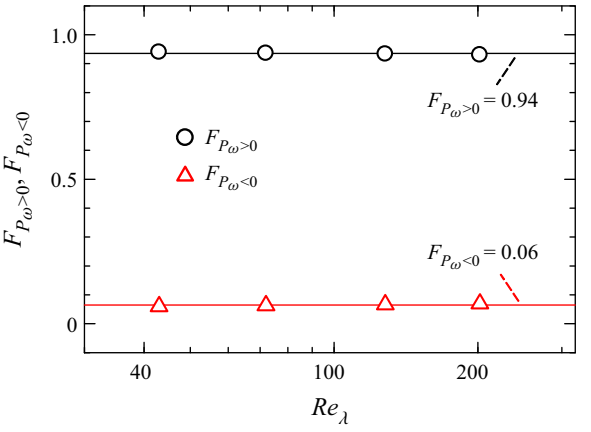

Figure 3. Fractions of shear layers with positive and negative enstrophy production $P_\omega = \omega_i S_{ij} \omega_j$, $F_{P_\omega>0}$ and $F_{P_\omega<0}$, as functions of the turbulent Reynolds number Re_λ.

opposite directions are observed on the sides of the thin shear layer. Therefore, the velocity in the ζ_3 direction, u_3, significantly varies across the shear layer. The characteristics of each shear layer are assessed with the profiles of u_3 and I_S along the ζ_2 axis at $(\zeta_1, \zeta_3) = (0, 0)$. Figure 2(*c*) presents the plots of u_3 and I_S across the shear layer visualised in figure 2(*b*). The Kolmogorov length and velocity scales, η and $u_\eta = (\nu\varepsilon_0)^{1/4}$, are used to normalise ζ_2 and u_3, respectively, whereas I_S is normalised by the shear intensity at $\zeta_2 = 0$, $I_{S,max}$. As the shear layer is thin in the ζ_2 direction, $I_S(\zeta_2)$ decreases rapidly with ζ_2 from the peak at $\zeta_2 = 0$. The layer thickness δ_S is evaluated as the half-width of I_S on the ζ_2 axis, namely the distance between two locations with $I_S(\zeta_2)/I_{S,max} = 0.5$ for $\zeta_2 > 0$ and $\zeta_2 < 0$. In addition, the velocity jump across the shear layer, u_S, is calculated with $\partial u_3/\partial\zeta_2$ at $\zeta_2 = 0$ as $u_S = (\partial u_3/\partial\zeta_2)\delta_S$. These length and velocity scales are also shown in figure 2(*c*). Then, the shear Reynolds number is defined as $Re_S = u_S\delta_S/\nu$. These definitions of u_S, δ_S and Re_S are applied for an instantaneous flow field around each shear layer whereas the length and velocity scales estimated from a mean flow field around the shear layers have been discussed in previous studies (Watanabe *et al.* 2020; Fiscaletti *et al.* 2021; Hayashi *et al.* 2021*a*).

The mean velocity profile around shear layers has shown that the shear layer appears in a biaxial strain field. The enstrophy production $P_\omega = \omega_i S_{ij} \omega_j$ actively occurs in the shear layers because of the interaction between the shear and biaxial strain (Buxton & Ganapathisubramani 2010; Elsinga & Marusic 2010; Eisma *et al.* 2015; Elsinga *et al.* 2017; Watanabe *et al.* 2020). However, some shear layers may have negative P_ω. The number of the identified local maxima of I_S is evaluated separately for $P_\omega > 0$ and $P_\omega < 0$, for which the numbers are denoted by $N_{P_\omega>0}$ and $N_{P_\omega<0}$, respectively. The fractions of shear layers with $P_\omega > 0$ and $P_\omega < 0$ are given by $F_{P_\omega>0} = N_{P_\omega>0}/N_{SH}$ and $F_{P_\omega<0} = N_{P_\omega<0}/N_{SH}$ with $N_{SH} = N_{P_\omega>0} + N_{P_\omega<0}$. Figure 3 plots $F_{P_\omega>0}$ and $F_{P_\omega<0}$ as functions of Re_λ. For all cases, $F_{P_\omega>0} \approx 0.94$ and $F_{P_\omega<0} \approx 0.06$ are obtained regardless of the Reynolds number. Almost all shear layers have positive enstrophy production. The primary interest of this paper is in the characteristics of strained shear layers with $P_\omega > 0$ for comparisons with Burgers' vortex layer and numerical simulations of an isolated shear layer in a biaxial strain field, both of which also have $P_\omega > 0$. Therefore, the statistics of u_S, δ_S and Re_S are calculated with ensemble averages of the shear layers with $P_\omega > 0$.

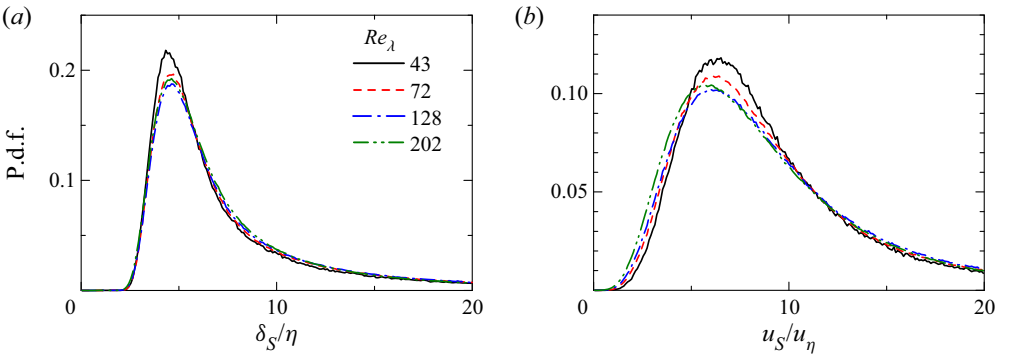

Figure 4. Probability density functions of (*a*) thickness δ_S and (*b*) velocity jump u_S of shear layers. The thickness and velocity jump are normalised by the Kolmogorov length and velocity scales, η and u_η, respectively.

2.3. *Thickness, velocity jump and Reynolds number of small-scale shear layers*

Variations of the shear layer characteristics are examined with the probability density functions (p.d.f.s) of δ_S, u_S and Re_S. Figure 4 shows the p.d.f.s of δ_S and u_S, which are normalised by the Kolmogorov length and velocity scales (η and u_η), respectively. The p.d.f.s hardly depend on Re_λ. Because of $u_\eta\eta/\nu = 1$, Re_S can be written as $Re_S = (u_S/u_\eta)(\delta_S/\eta)$. Therefore, the p.d.f.s of δ_S/η and u_S/u_η suggest that Re_S hardly depends on Re_λ and the behaviour of typical small-scale shear layers in turbulence can be insensitive to the flow Reynolds number. However, the Reynolds number dependence can be important for intense shear layers because an extremely large velocity gradient tends to be observed at a very high Reynolds number (Elsinga *et al.* 2017; Buaria *et al.* 2019; Das & Girimaji 2020; Ghira *et al.* 2022).

The Re_S dependence of δ_S and u_S is examined with the joint p.d.f.s of $(\delta_S/\eta, Re_S)$ and $(u_S/u_\eta, Re_S)$ in figure 5(*a*,*b*), respectively. Here, the results for NS2 are presented because the Re_λ dependence is weak when the Kolmogorov scales are used for normalisation. The Reynolds number Re_S is positively correlated with δ_S and u_S, as expected from the definition of $Re_S = u_S\delta_S/\nu$. The highest probability is observed for $(\delta_S/\eta, Re_S) \approx (4, 20)$ and $(u_S/u_\eta, Re_S) \approx (5, 20)$, suggesting that the shear layers in turbulence typically have $(\delta_S/\eta, u_S/\eta, Re_S) \approx (4, 5, 20)$ although variations from these values are confirmed from the distributions of the joint p.d.f.s. Specifically, the shear Reynolds number Re_S ranges approximately between 10 and 70.

The relation between the shear layer and the nearby strain field in turbulence agrees with Burgers' vortex layer (Watanabe *et al.* 2020), which is one of the exact steady solutions of Navier–Stokes equations for a uniform shear layer subject to a biaxial strain (Burgers 1948; Davidson 2004). In both shear layers in turbulence and Burgers' vortex layer, a compressive strain acts in the normal direction of the shear layer while an extensive strain acts in the vorticity direction of the shear. For Burgers' vortex layer, the half-width of I_S is related to the strain rate α as $\delta_{BV} = 1.67\sqrt{2\nu/\alpha}$. The strain rate acting on vortices is often estimated as $\alpha = \omega_i S_{ij}\omega_j/\omega_k\omega_k$, for which the diameter of Burgers' vortex has been compared with the actual diameter of vortex tubes (Jiménez & Wray 1998; da Silva *et al.* 2011; Jahanbakhshi *et al.* 2015; Watanabe *et al.* 2017*b*; Ghira *et al.* 2022). Similarly, δ_{BV} is evaluated with α at $(\zeta_1, \zeta_2, \zeta_3) = (0, 0, 0)$ for each shear layer and is compared with the half-width of I_S, δ_S. Here, the Re_S dependence of the relation between δ_S and δ_{BV} is examined with the present DNS database, whereas a general comparison between δ_S and

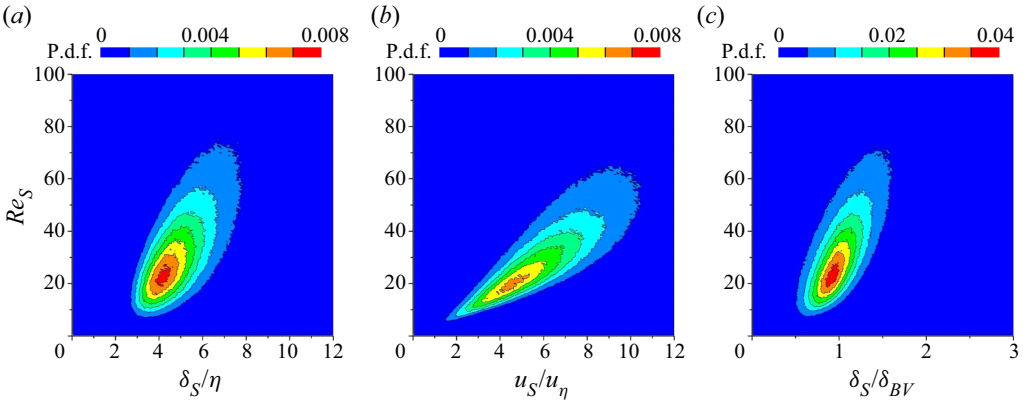

Figure 5. Joint probability density functions of (*a*) $(\delta_S/\eta, Re_S)$, (*b*) $(u_S/u_\eta, Re_S)$ and (*c*) $(\delta_S/\delta_{BV}, Re_S)$ of shear layers in NS2. Here, the shear layer thickness δ_S is normalised with the Kolmogorov scale η or the thickness of Burgers' vortex layer $\delta_{BV} = 1.67\sqrt{2\nu/\alpha}$ calculated with the strain rate $\alpha = \omega_i S_{ij}\omega_j/\omega_k\omega_k$ while the velocity jump u_S is normalised by the Kolmogorov velocity scale u_η.

δ_{BV} has been provided for isotropic turbulence and planar jets in Watanabe *et al.* (2020) and Hayashi *et al.* (2021*a*). Figure 5(*c*) shows the joint p.d.f. between δ_S/δ_{BV} and Re_S. For the typical shear Reynolds number $Re_S \approx 20$, the joint p.d.f. reaches the maximum for $\delta_S/\delta_{BV} \approx 1$, implying that the relation between the layer thickness and the strain rate is consistent with Burgers' vortex layer. The p.d.f. also shows that δ_S/δ_{BV} is positively correlated with Re_S. Thus, the layer thickness tends to be larger than that of Burgers' vortex layer at large Re_S, and *vice versa*. An unsteady analysis of Burgers' vortex layer predicts that the layer thickness asymptotically approaches δ_{BV} with time when the initial thickness differs from δ_{BV} (Davidson 2004). Therefore, the shear layers with large Re_S are possibly being flattened with time due to the compressible strain while those with small Re_S are thickened via the viscous effect. In addition, the p.d.f. is distributed for $0.5 \lesssim \delta_S/\delta_{BV} \lesssim 1.5$ and most shear layers in isotropic turbulence are close to an equilibrium state in terms of the relation between the thickness and the strain rate.

These probability distributions of length and velocity scales are consistent with previous studies of a mean flow in a reference frame defined with the eigenvectors of the rate-of-strain tensor (Elsinga & Marusic 2010; Elsinga *et al.* 2017). This reference frame is often referred to as a strain eigenframe. These studies introduce the strain eigenframe at each point of the flow and take averages of various quantities as functions of the position in the strain eigenframe. This approach is similar to the present method, which relies on the local reference frame defined with $\boldsymbol{\nabla u}_S$. Even though the averages in the strain eigenframe are not taken for shear layers, a mean flow profile in the strain eigenframe also exhibits a shear-layer pattern (Elsinga & Marusic 2010), which is similar to the mean flow around the shear layers (Watanabe & Nagata 2022). The p.d.f. of shear intensity I_S in isotropic turbulence and turbulent jets indicates that shearing motions appear anywhere in turbulence (Nagata *et al.* 2020; Hayashi *et al.* 2021*a*). For this reason, the statistics of turbulence can be strongly influenced by shearing motions, and therefore, the averages in the strain eigenframe taken for an entire turbulent region is consistent with those taken solely for shear layers. The present study examines the length and velocity scales of each shear layer with their probability distribution and confirms that the most typical values of the half-width and velocity jump of the shear layers are $\delta_S/\eta \approx 4$ and $u_S/u_\eta \approx 5$, respectively. Similarly, the shear layer of the mean flow in the strain eigenframe has a

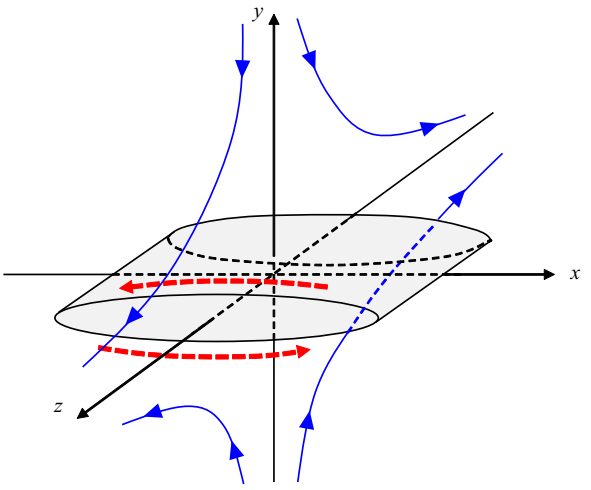

Figure 6. An isolated shear layer with a finite aspect ratio in a biaxial strain field.

full width of about 10η and a velocity jump of about $6u_\eta$. The p.d.f. in figure 4 confirms that some shear layers have different velocity and length scales from the typical values. However, the mean flow in the strain eigenframe is strongly dominated by the most typical shear layers with $\delta_S/\eta \approx 4$ and $u_S/u_\eta \approx 5$.

3. Numerical simulations of an isolated shear layer in a biaxial strain field

3.1. *The model of an isolated shear layer*

Numerical simulations are performed for an isolated shear layer in a biaxial strain field illustrated in figure 6. This simple model is an approximation of the mean-flow pattern observed around the small-scale shear layers in turbulence (Watanabe *et al.* 2020; Hayashi *et al.* 2021*a*; Watanabe & Nagata 2022), which also resembles the shear-layer pattern observed in a mean flow with a strain eigenframe taken regardless of the presence of shear layers (Elsinga & Marusic 2010; Elsinga *et al.* 2017). The model assumes that the aspect ratio of the length scales in the x and y directions is finite. The simulations are carried out to investigate the response of the shear layer to perturbations. Some physical parameters are determined based on the shear layer characteristics in isotropic turbulence presented in § 2 to relate the behaviour of the isolated shear layer to that of small-scale shear layers in turbulence. The shear coordinates, ζ_1, ζ_2 and ζ_3, used in § 2 are respectively related to z, y and x in figure 6. The model follows the numerical study of a row of alternating vortex sheets in a biaxial strain field (Lin & Corcos 1984) although the present study considers a single isolated shear layer. In this section, a dimensional variable is denoted with a symbol with a tilde, e.g. $\tilde{f}$, whose non-dimensional counterpart is f. The model assumes an incompressible fluid. The transverse and vorticity directions of the shear layer are denoted by $\tilde{y}$ and $\tilde{z}$, respectively. The shear layer is initially parallel to the $\tilde{x}$ direction. The shear layer is subject to a biaxial strain with compression in the $\tilde{y}$ direction and stretching in the $\tilde{z}$ direction. The velocity components in the $\tilde{x}$, $\tilde{y}$ and $\tilde{z}$ directions are denoted by $\tilde{u}$, $\tilde{v}$ and $\tilde{w}$, respectively. The origin of the coordinate system is located at the centre of the shear layer.

The initial velocity field $\tilde{\boldsymbol{u}} = (\tilde{u}, \tilde{v}, \tilde{w})$ can be decomposed into the components of a base flow and perturbations as $\tilde{\boldsymbol{u}} = \tilde{\boldsymbol{u}}_B + \tilde{\boldsymbol{u}}'$. In addition, the base flow, $\tilde{\boldsymbol{u}}_B$, is further decomposed into the components associated with the strain and vorticity as $\tilde{\boldsymbol{u}}_B = \tilde{\boldsymbol{u}}_S + \tilde{\boldsymbol{u}}_V$,

the latter of which can be defined with the vorticity profile. The present model assumes that an initial profile of vorticity is given by

$$\tilde{\omega}_x(\tilde{x},\tilde{y},\tilde{z})=0;\quad \tilde{\omega}_y(\tilde{x},\tilde{y},\tilde{z})=0;\quad \tilde{\omega}_z(\tilde{x},\tilde{y},\tilde{z})=\omega_0\exp\left(-\frac{\tilde{y}^2}{\delta^2}\right)\exp\left[-\frac{\tilde{x}^2}{(A_R\delta)^2}\right]. \tag{3.1a–c}$$

Here, ω_0 is the peak vorticity at the centre of the shear layer, A_R is the aspect ratio and δ is the shear layer thickness. The velocity components for the time-independent biaxial strain, $\tilde{\boldsymbol{u}}_S=(\tilde{u}_S,\tilde{v}_S,\tilde{w}_S)$, are given by

$$\tilde{u}_S(\tilde{x},\tilde{y},\tilde{z})=0,\quad \tilde{v}_S(\tilde{x},\tilde{y},\tilde{z})=-\gamma\tilde{y},\quad \tilde{w}_S(\tilde{x},\tilde{y},\tilde{z})=\gamma\tilde{z} \tag{3.2a–c}$$

with a constant strain rate γ, which is assumed to satisfy the equilibrium relation $\gamma=2\nu/\delta^2$ of Burgers' vortex layer. The DNS results in § 2 have suggested that the majority of shear layers in turbulence approximately satisfy this relation. For the vorticity profile of (3.1*a–c*), $w_V=0$ is satisfied anywhere. The remaining components $(\tilde{u}_V,\tilde{v}_V)$ are determined as $(\tilde{u}_V,\tilde{v}_V)=(-\partial\tilde{\phi}/\partial\tilde{y},\partial\tilde{\phi}/\partial\tilde{x})$ with a vector potential $\tilde{\phi}$ which satisfies $\tilde{\omega}_z=\nabla^2\tilde{\phi}$. For $A_R\to\infty$, (3.1*a–c*) and (3.2*a–c*) express Burgers' vortex layer, which is infinitely long in the x direction. A similar vorticity profile was also used in Lin & Corcos (1984), where a cosine function was used instead of $\exp[-\tilde{x}^2/(A_R\delta)^2]$ to model the row of shear layers with positive and negative spanwise vorticities. Their model allows the interaction between adjacent shear layers, which is observed in the development of a plane mixing layer, whereas this interaction does not occur in the present model of the isolated shear layer because the simulations are designed to investigate the development of a single shear layer under perturbations.

The perturbations $\tilde{\boldsymbol{u}}'$ are defined based on the spanwise-vorticity perturbations $\tilde{\omega}_z'$, whose profile is given by

$$\tilde{\omega}_z'(\tilde{x},\tilde{y},\tilde{z})=\omega_0'\sin\left[2\pi\left(\frac{\tilde{x}}{\Lambda}+\varphi_x\right)\right]\sin\left[2\pi\left(\frac{\tilde{y}}{\Lambda}+\varphi_y\right)\right]G(\tilde{x},\tilde{y}), \tag{3.3}$$

$$G(\tilde{x},\tilde{y})=\left[\frac{1}{2}+\frac{1}{2}\tanh\left(\frac{L_{xf}-2|\tilde{x}|}{12\delta}\right)\right]\left[\frac{1}{2}+\frac{1}{2}\tanh\left(\frac{L_{yf}-2|\tilde{y}|}{12\delta}\right)\right], \tag{3.4}$$

where Λ and ω_0' are the wavelength and amplitude, respectively, whereas φ_x and φ_y are the phases of the perturbations. The top-hat function $G(\tilde{x},\tilde{y})$ is equal to 1 near the shear layer and becomes 0 in the far field. Therefore, the sinusoidal perturbations exist only for $|\tilde{x}|\lesssim L_{xf}/2$ and $|\tilde{y}|\lesssim L_{yf}/2$. Once the profile of the vorticity perturbations is determined, $(\tilde{u}',\tilde{v}',\tilde{w}')=(-\partial\tilde{\phi}'/\partial\tilde{y},\partial\tilde{\phi}'/\partial\tilde{x},0)$ is calculated with a vector potential $\tilde{\phi}'$ which satisfies $\tilde{\omega}_z'=\nabla^2\tilde{\phi}'$. The profile of $(\tilde{u}',\tilde{v}')$ exhibits fluctuations around $(\tilde{u}',\tilde{v}')=(0,0)$, where the maximum amplitude is denoted by u_0'. Because ω_0' is directly related to u_0', the numerical parameter is determined by specifying u_0'. This can be done by generating $(\tilde{u}',\tilde{v}')$ from (3.3) and (3.4) with given values of Λ and ω_0'. Then, $(\tilde{u}',\tilde{v}')$ are normalised such that the maximum value of $\tilde{u}'$ is equal to u_0'.

Numerical simulations are performed with governing equations non-dimensionalised with reference velocity and length scales, u_r and l_r, e.g. $u=\tilde{u}/u_r$ and $\omega_z=\tilde{\omega}_z/(u_r/l_r)$. Time $\tilde{t}$ can also be non-dimensionalised as $t=\tilde{t}/t_r$ with the reference time scale $t_r=l_r/u_r$. Here, u_r and l_r are given by $u_r=\sqrt{\pi}\omega_0\delta$ and $l_r=\delta$. The choice of u_r is based on Burgers' vortex layer, where the velocity jump across the layer is given by $\sqrt{\pi}\omega_0\delta$.

3.2. *Governing equations, numerical methods and parameters*

The present model assumes that the initial profiles of u and v are independent of z. In this case, u and v remain independent of z even after the shear layer development (Lin & Corcos 1984). Therefore, the continuity and momentum equations non-dimensionalised by u_r and l_r are written as

$$\frac{\partial u}{\partial x}+\frac{\partial v}{\partial y}=-\frac{2}{Re}, \tag{3.5}$$

$$\frac{\partial u}{\partial t}+u\frac{\partial u}{\partial x}+v\frac{\partial u}{\partial y}=-\frac{\partial p}{\partial x}+\frac{1}{Re}\left(\frac{\partial^2 u}{\partial x^2}+\frac{\partial^2 u}{\partial y^2}\right), \tag{3.6}$$

$$\frac{\partial v}{\partial t}+u\frac{\partial v}{\partial x}+v\frac{\partial v}{\partial y}=-\frac{\partial p}{\partial y}+\frac{1}{Re}\left(\frac{\partial^2 v}{\partial x^2}+\frac{\partial^2 v}{\partial y^2}\right), \tag{3.7}$$

$$\frac{\partial w}{\partial t}=0, \tag{3.8}$$

with the Reynolds number $Re=u_r l_r/\nu=\sqrt{\pi}\omega_0\delta^2/\nu$. Here, $2/Re$ on the right-hand side of (3.5) is obtained from $\partial w/\partial z=\gamma/(u_r/l_r)$ with $\gamma=2\nu/\delta^2$.

Solving these equations yields the temporal evolution of the shear layer initialised with the velocity profile explained above. As u and v are independent of z and w remains unchanged with time, the simulations can be conducted in a two-dimensional computational domain. The governing equations are solved with an in-house finite-difference code, which is developed by reducing the dimension of our DNS code from three to two. The original DNS code was used for various turbulent flows in our previous studies, where the code was validated by comparisons with experiments and other numerical simulations (e.g. Watanabe & Nagata 2018; Watanabe, Zhang & Nagata 2019; Katagiri, Watanabe & Nagata 2021; Watanabe, Zheng & Nagata 2022). The code is the same as that used for isotropic turbulence except for spatial discretisation, for which a second-order fully conservative finite-difference scheme is employed (Morinishi *et al.* 1998).

The isolated shear layer is simulated in a rectangular domain with a size of $(L_x, L_y)=(250\delta, 250\delta)$, which is much larger than the shear layer. Therefore, the boundary conditions assume the far-field condition of the base flow. Here, $u=0$ is applied at all boundaries. The zero-gradient condition is applied to v at the boundaries in the x direction while $\tilde{v}=-\gamma\tilde{y}$ is used for the y direction. The computational domain is discretised with $(N_x\times N_y)=(300\times 300)$ grid points. A non-uniform grid is employed to achieve a high spatial resolution near the shear layer. Here, x and y positions of the grid are determined with integers i and j by the following mapping functions:

$$\tilde{x}(i)=-\frac{L_x}{2\alpha_x}\mathrm{atanh}\left[(\tanh\alpha_x)\left(1-\frac{2i}{N_x}\right)\right]\quad\text{with } i=0,\ldots,N_x, \tag{3.9}$$

$$\tilde{y}(j)=-\frac{L_y}{2\alpha_y}\mathrm{atanh}\left[(\tanh\alpha_y)\left(1-\frac{2j}{N_y}\right)\right]\quad\text{with } j=0,\ldots,N_y, \tag{3.10}$$

with $\alpha_x=\alpha_y=3.5$. The grid size becomes large as being away from the centre of the domain. The distribution of the grid size for these functions can be found in Watanabe *et al.* (2018). A non-dimensional time increment is $\Delta t=0.025$, and time is advanced until $t=50$ in each simulation.

The numerical simulations are performed for various sets of the Reynolds number Re, the aspect ratio A_R and the perturbation wavelength Λ. Table 2 summarises Re and A_R

Re	A_R	δ_S/δ	u_S/u_r	Re_S
15	10	1.68	0.85	22
15	30	1.69	0.91	23
30	10	1.68	0.85	43
30	30	1.69	0.91	46
45	10	1.68	0.85	65
45	30	1.69	0.91	69

Table 2. Parameters of numerical simulations of an isolated shear layer in a biaxial strain field: the Reynolds number $Re = u_r l_r/\nu$ defined with reference scales of the simulations, the aspect ratio of the shear layer A_R, the ratio between the half-width of I_S and the layer thickness δ_S/δ, the velocity scale ratio u_S/u_r and the shear Reynolds number $Re_S = u_S\delta_S/\nu$.

considered in this study. Here, these simulations consider $\varphi_x = \varphi_y = 0$ while the influence of the phases is investigated with additional simulations, as explained below. The Reynolds number is determined based on the DNS data while $A_R = 10$ and 30 are chosen to discuss two different types of the evolution of the shear layer. In turbulent flows, A_R differs for each shear layer as confirmed from visualisations of shear layers in figure 1 and previous studies (Nagata *et al.* 2020; Fiscaletti *et al.* 2021; Hayashi *et al.* 2021*b*). We have noticed that it is difficult to quantify the aspect ratio which can be directly compared with A_R of the ideal numerical model because of the curved shape of shear layers in turbulence. In figure 2(*b*), the shear layer extends approximately from $\zeta_3/\eta = -15$ to 30 whereas the thickness is about 4η. Thus, the aspect ratio is close to 10. Visualisation of shear intensity I_S or shear vorticity $|\boldsymbol{\omega}_S|$ in isotropic turbulence and turbulent free shear flows has suggested that the aspect ratio of some shear layers is close to or smaller than about 10 (Fiscaletti *et al.* 2021; Hayashi *et al.* 2021*a*; Watanabe & Nagata 2022). However, these studies have also observed shear layers with a larger aspect ratio than 10. A long shear layer is broken during the roll-up and generates more than one shear layer with small A_R around a vortex tube (Horiuti & Takagi 2005; Watanabe *et al.* 2020). This might be the reason why the shear layers with a wide range of A_R are observed in turbulence. Therefore, instead of matching the aspect ratio, two cases of $A_R = 10$ and 30 are considered because the shear layer behaves differently for large and small A_R. In the numerical simulations of the isolated shear layer, Re is defined with the layer thickness δ in (3.1*a–c*) and the velocity difference $u_r = \sqrt{\pi}\omega_0\delta$ across the layer. On the other hand, the DNS results of isotropic turbulence have been examined with the shear Reynolds number Re_S defined with the half-width of the shear intensity, δ_S, and the velocity jump u_S defined with δ_S and the local velocity gradient in the shear layer. Table 2 also lists δ_S/δ, u_S/u_r and the shear Reynolds number Re_S evaluated with the same definitions of δ_S and u_S as in the DNS of isotropic turbulence. The present simulations consider $20 \lesssim Re_S \lesssim 70$, which is determined from the p.d.f. of Re_S in the isotropic turbulence. For each set of (Re, A_R), the simulations are performed for the perturbation wavelength $\Lambda/\delta = 8, 12, \ldots$ or 40 to examine the wavelength dependence. The amplitude of velocity fluctuations is fixed in all simulations as $u_0'/u_r = 0.1$, for which the results are compared with unperturbed cases ($u_0' = 0$). For $G(x, y)$ in (3.4), $L_{xf} = 125\delta$ and $L_{yf} = 100\delta$ are used for the perturbations to cover a large area around the shear layer.

A uniform shear layer with $A_R = \infty$ is also investigated for a comparison with the finite A_R cases. The initial vorticity profile is (3.1*a–c*) with $A_R \to \infty$. The periodic boundary condition is applied in the x direction. The region of the perturbations is given by (3.4) with $L_{xf} \to \infty$. The uniform shear layer is simulated for $Re = 30$ with perturbations with

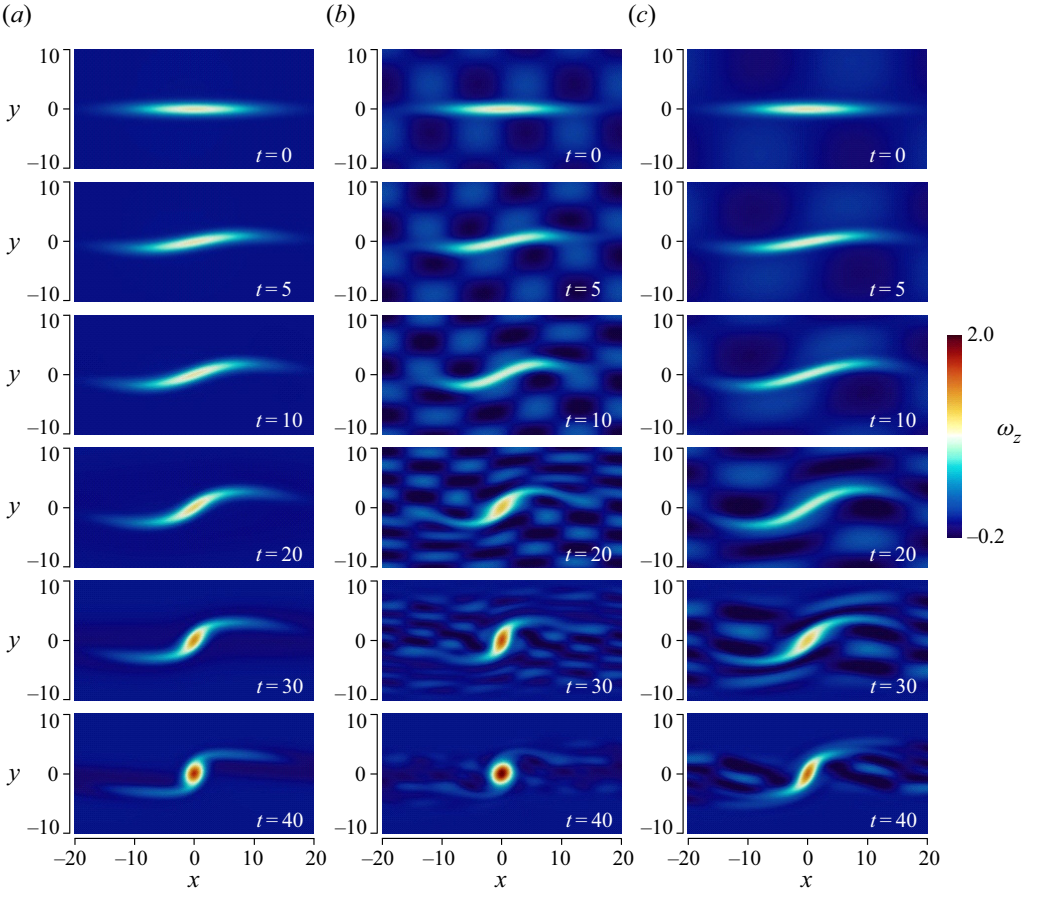

Figure 7. Temporal evolutions of an isolated shear layer in a biaxial strain field with the aspect ratio $A_R = 10$ and the Reynolds number $Re = 30$: (*a*) unperturbed case ($u_0' = 0$); perturbed cases with (*b*) $u_0'/u_r = 0.1$ and $\Lambda/\delta = 16$ and (*c*) $u_0'/u_r = 0.1$ and $\Lambda/\delta = 32$. From top to bottom, time increases as $t = 0$, 5, 10, 20, 30 and 40. Only a small part of the computational domain is shown here.

$u_0'/u_r = 0.1$ and $\Lambda/\delta = 8, 12, \ldots$ or 40. As the perturbations should also be periodic in the x direction, the domain size is determined with Λ as $(L_x, L_y) = (4\Lambda, 250\delta)$. The grid spacing in the x direction is uniform, and N_x is determined such that the spacing is 0.2δ. Other parameters and conditions are the same for both infinite- and finite-A_R cases.

3.3. *Temporal development of an isolated shear layer*

Figure 7 shows the profiles of vorticity ω_z to visualise the temporal evolution of a shear layer with a low aspect ratio ($A_R = 10$). The unperturbed case with $u_0' = 0$ is shown in figure 7(*a*) while the perturbed cases with the wavelength of $\Lambda/\delta = 16$ and 32 are shown in figure 7(*b*,*c*). In all cases, the initially flat shear layer is distorted with time and forms a circular region with large vorticity. The formation of the vortex occurs even in the unperturbed case. This is caused by the self-induced velocity of the shear layer with the low aspect ratio. The sheet-like distribution of vorticity accompanies the upward and downward velocities on the right and left of the shear layer, respectively (Lin & Corcos 1984). Consequently, the shear layer is distorted by itself and generates the vortex centred

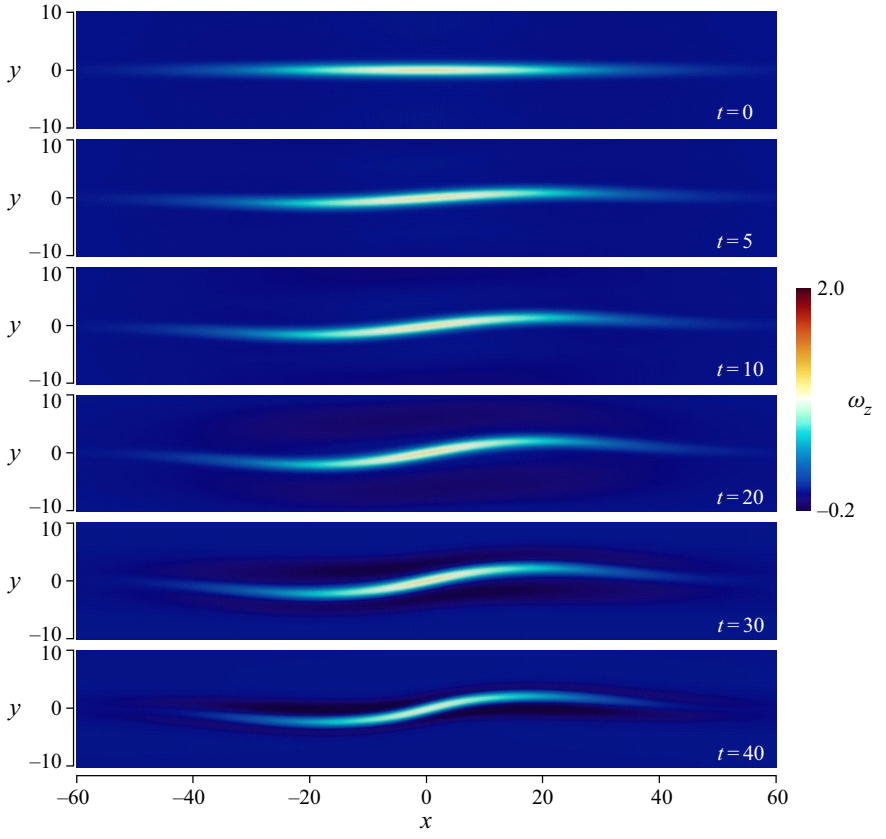

Figure 8. Temporal evolution of an unperturbed isolated shear layer in a biaxial strain field with the aspect ratio $A_R = 30$, the Reynolds number $Re = 30$ and $u_0'/u_r = 0$. From top to bottom, time increases as $t = 0$, 5, 10, 20, 30 and 40. Only a small part of the computational domain is shown here.

at $(x, y) = (0, 0)$. A similar formation of the vortex is also observed in the perturbed cases in figure 7(*b*,*c*). However, the time required for the vortex formation is different among the three cases. At $t = 40$, the value of ω_z in the vortex for the unperturbed case is smaller and larger than those for the perturbed cases with $\Lambda/\delta = 16$ and 32, respectively. In addition, as the vortex forms at $t = 30$ and 40, the shape of the large-ω_z region changes from an ellipse to a circular shape. Compared with the unperturbed case, the vortex formation is accelerated for the perturbations with $\Lambda/\delta = 16$ whereas it is delayed for $\Lambda/\delta = 32$.

Figure 8 shows the temporal evolution of a shear layer with a high aspect ratio ($A_R = 30$) without perturbations whereas the perturbed cases with $\Lambda/\delta = 16$ and 32 are visualised in figures 9 and 10, respectively. Unlike the shear layer with small A_R, the vortex formation does not occur for the unperturbed case with large A_R in figure 8. The vortices form in the shear layer with perturbations with $\Lambda/\delta = 16$ in figure 9, where three vortices can be found at $t = 40$. However, the perturbations with a twice-as-large wavelength, $\Lambda/\delta = 32$, are not effective to trigger the formation of vortices, as shown in figure 10. The vortex formation for $\Lambda/\delta = 16$ is initiated with the distortion of the shear layer by the perturbations, and its process is more similar to Kelvin–Helmholtz instability (Patnaik *et al.* 1976) than that for the low A_R case in figure 7.

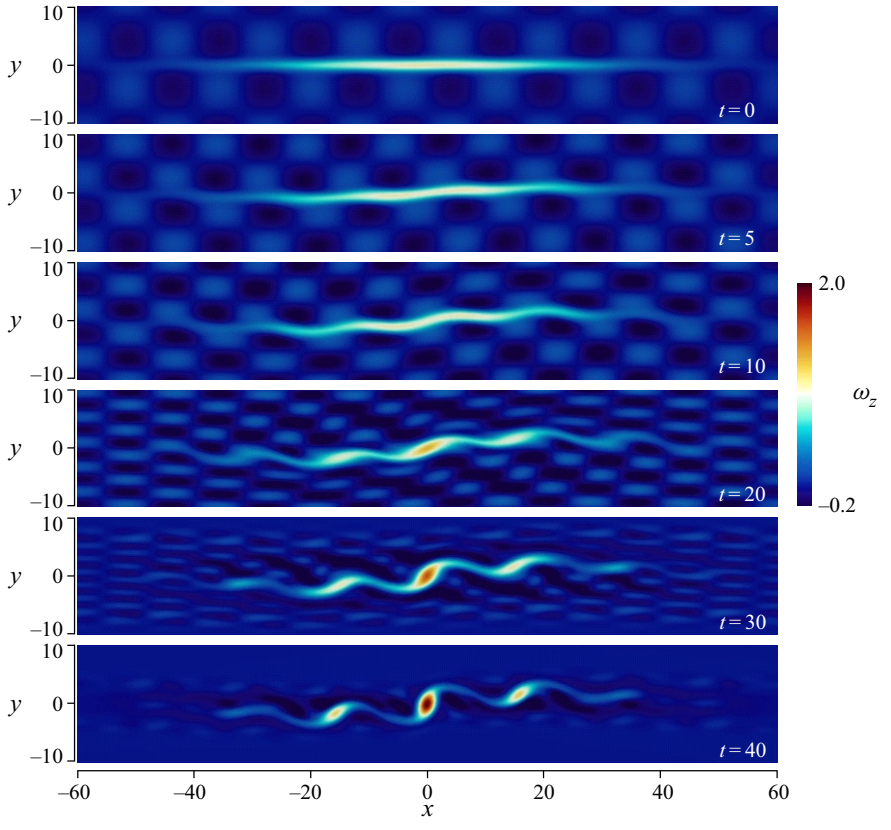

Figure 9. The same as figure 8 but for a perturbed case with $u_0'/u_r = 0.1$ and $\Lambda/\delta = 16$.

When the vortices are successfully formed in the shear layer, the maximum vorticity ω_{max} in the shear layer increases with time. Figure 11 shows the temporal variation of ω_{max} of the shear layers with $Re = 30$ for different Λ and A_R. The results are not shown for all values of Λ for visibility of the figure while Λ dependence is examined in detail at several time instances below. For the low aspect ratio with $A_R = 10$ in figure 11(a), ω_{max} increases for both unperturbed and perturbed cases with all wavelengths because of the vortex formation. The growth of ω_{max} occurs rapidly by the perturbations for $A_R/\delta = 12$ and 16 whereas it is delayed for larger wavelengths. For the high aspect ratio in figure 11(b), ω_{max} without perturbations does not vary until $t \approx 30$ and then begins to decrease. The increase of ω_{max} can be seen for the perturbed case with $\Lambda/\delta = 12$, 16 and 24. The perturbations with larger Λ do not cause a continuous increase of ω_{max} and result in the decay at a late time for $\Lambda/\delta = 32$ and 40. For both aspect ratios, the perturbations with $\Lambda/\delta = 12$ and 16 are effective to promote the vortex formation, which does not occur or is delayed for larger Λ.

The above results are obtained for $Re = 30$ whereas the Reynolds number dependence is examined in figures 12 and 13, where the vorticity ratio ω_r between $\omega_{max}(t)$ and its initial value is plotted as a function of Λ/δ for three Reynolds numbers at $t = 20$, 30 and 50. When the vortex formation occurs in the shear layer and the spanwise vorticity is amplified, ω_r increases with time. On the other hand, the increase of ω_r does not occur when the shear layer is simply distorted without vortex formation. The results for $A_R = 10$ at $t = 20$, 30 and 50 are shown in figures 12(a), 12(b) and 12(c), respectively. For comparison, ω_r for the

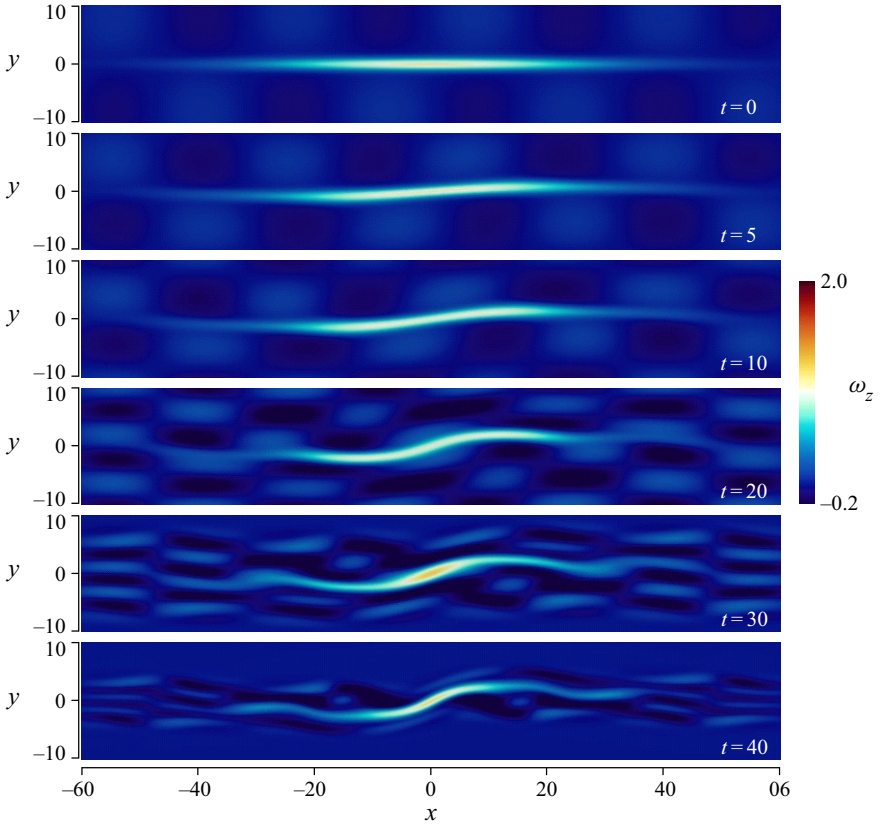

Figure 10. The same as figure 8 but for a perturbed case with $u_0'/u_r = 0.1$ and $\Lambda/\delta = 32$.

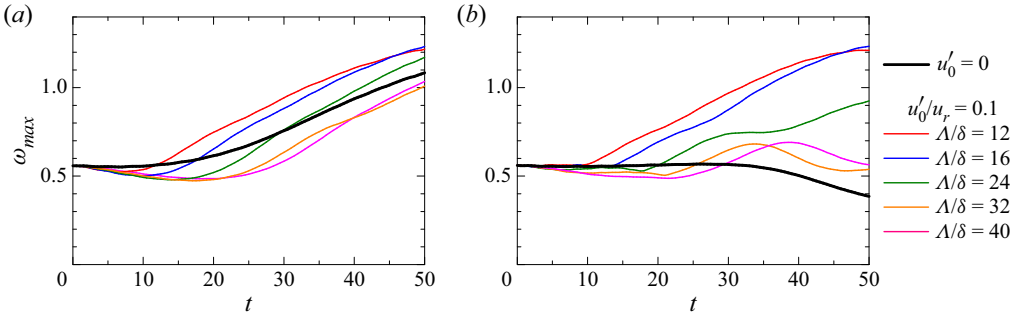

Figure 11. Temporal variations of the maximum vorticity ω_{max} of the isolated shear layer with $Re = 30$ and (*a*) $A_R = 10$ and (*b*) $A_R = 30$.

unperturbed case is plotted at $\Lambda = 0$. As the vortex formation occurs without perturbations for $A_R = 10$, ω_r gradually increases with time even without perturbations. However, the rapid growth of ω_r is observed for the perturbations with $\Lambda/\delta \approx 12$, for which ω_r tends to be large compared with other values of Λ/δ. At each time instance, ω_r decreases from the peak of ω_r at $\Lambda/\delta = 8$–16 as Λ/δ increases. In addition, ω_r for $\Lambda/\delta = 8$ is smaller than those for $\Lambda/\delta = 12$ at $t = 30$ and 50 in figure 12(*b*,*c*) except for $Re = 45$ at $t = 30$.

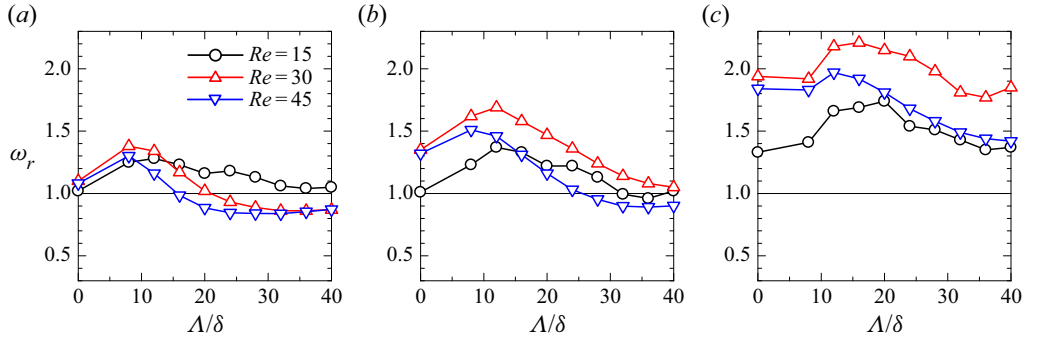

Figure 12. Wavenumber dependence of maximum vorticity normalised by its initial value, $\omega_r = \omega_{max}(t)/\omega_{max}(t=0)$ for the aspect ratio $A_R = 10$. The results taken at (*a*) $t = 20$, (*b*) $t = 30$ and (*c*) $t = 50$ are plotted as functions of the perturbation wavelength Λ/δ.

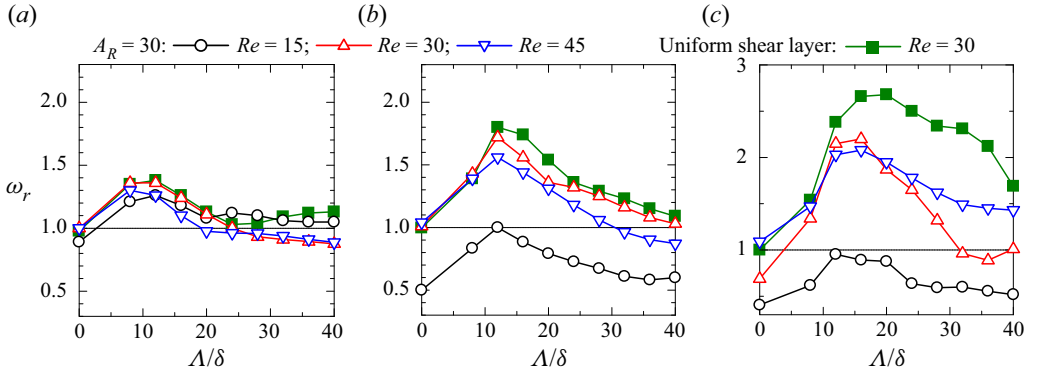

Figure 13. The same as figure 12 but for $A_R = 30$: (*a*) $t = 20$, (*b*) $t = 30$ and (*c*) $t = 50$. The results for the uniform shear layer ($A_R \to \infty$) with $Re = 30$ are also shown for comparison.

Therefore, the perturbations with $\Lambda/\delta \approx 12$ more effectively cause the amplification of vorticity than those with larger or smaller Λ/δ. This wavelength dependence is similar for all Re. Figure 13 shows the results for $A_R = 30$, for which perturbations are necessary for the vortex formation. The results for the uniform shear layer ($A_R \to \infty$) with $Re = 30$ are also shown for comparison. For $Re = 30$, the Λ dependence of ω_r is similar for the isolated shear layer with $A_R = 30$ and the uniform shear layer. Therefore, the effects of the finite aspect ratio are not significant for $A_R = 30$, except for a late time. The wavelength dependence of the growth of ω_r for $A_R = 30$ is stronger than that for $A_R = 10$, especially at $t = 50$. As also found for $A_R = 10$, ω_r is large for $\Lambda/\delta \approx 12$, and the perturbations with larger or smaller Λ/δ do not cause the rapid increase of ω_r. A different trend is observed for $Re = 15$, for which ω_r decreases with time for the unperturbed case shown at $\Lambda/\delta = 0$. In figure 11(*b*), ω_{max} for $u_0' = 0$ does not vary with time until $t = 30$ and decreases for a later time. This decrease is also observed for $Re = 15$, resulting in $\omega_r < 1$ in figure 13. However, we note that the vortex formation with the amplification of ω_z occurs for the perturbed cases with $12 \leq \Lambda/\delta \leq 20$ and $Re = 15$. Therefore, ω_r for $12 \leq \Lambda/\delta \leq 20$ is larger than those for the unperturbed case and for larger or smaller Λ/δ. In summary, the perturbations with $\Lambda/\delta \approx 12$ tend to amplify the spanwise vorticity for all Re and A_R considered here. This wavelength of $\Lambda/\delta = 12$ corresponds to $\Lambda/\delta_S \approx 7.2$, where δ_S is

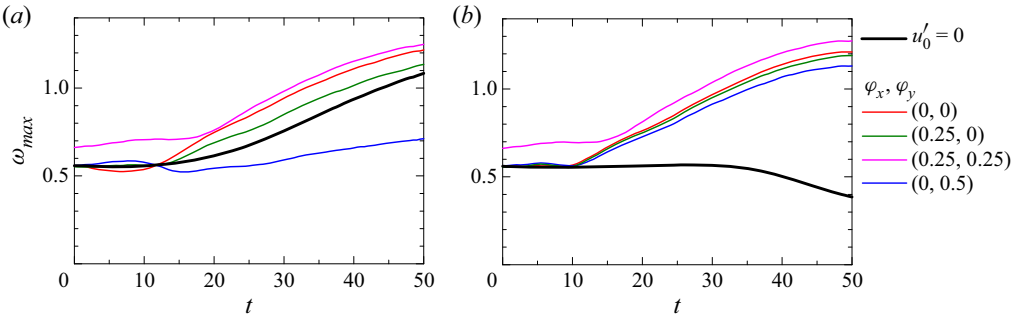

Figure 14. The effects of the phases of perturbations on the shear layer development for (*a*) $A_R = 10$ and (*b*) $A_R = 30$.

the half-width of shear intensity used in the shear layer analysis for isotropic turbulence and is related to δ as presented in table 2.

Simulations with $(\varphi_x, \varphi_y) \neq (0, 0)$ are also performed for the shear layer with $Re = 30$ and $A_R = 10$ or 30 and the perturbations with $\Lambda/\delta = 12$. All computational parameters except the phases are the same as in the other simulations. Figure 14 shows the temporal variations of the maximum vorticity ω_{max} for various values of φ_x and φ_y. The result for the unperturbed case ($u_0' = 0$) is also shown for comparison. For $\varphi_y = 0.25$, the spanwise vorticity of the perturbations is not zero at the centre of the shear layer and affects the initial value of ω_{max}. Except for $(\varphi_x, \varphi_y) = (0, 0.5)$ and $A_R = 10$, ω_{max} in the perturbed cases increases with time. For $A_R = 10$, the perturbations with $(\varphi_x, \varphi_y) = (0, 0.5)$ result in a slow growth of ω_{max}. The formation of the vortex is initially caused by the self-induced velocity of the shear layer with the low aspect ratio. The perturbations given with $(\varphi_x, \varphi_y) = (0, 0.5)$ negate the self-induced velocity associated with a positive spanwise vorticity because of the matched phase of velocity distribution. Therefore, the self-induced velocity does not effectively distort the shear layer. The growth of ω_{max} for $A_R = 30$ is observed regardless of the phases because the vortex formation begins with the distortion of the shear layer by the perturbations rather than the self-induced velocity.

The wavenumber dependence of the isolated shear layer with a finite aspect ratio A_R agrees with previous studies of a parallel shear flow with $A_R \to \infty$. A comparison between parallel shear flows with and without a biaxial strain suggests that the most unstable mode of the shear instability is hardly influenced by the strain in Burgers' vortex layer (Lin & Corcos 1984). The non-dimensional wavenumber in the linear stability analysis is often written as $\alpha = 2\pi\delta/\Lambda$. The maximum initial growth rate of the instability of Burgers' vortex layer was found for $\alpha \approx 0.40$–0.43, which slightly increases with the Reynolds number (Lin & Corcos 1984). These values of α correspond to $\Lambda/\delta \approx 15$, which is close to the wavelength for which the vorticity in the isolated shear layer rapidly grows ($\Lambda/\delta \approx 12$) in figures 12 and 13. Therefore, the wavelength dependence observed for the shear layer with a finite A_R can be related to the instability of the uniform shear layer with $A_R \to \infty$. One of the important differences is the vortex formation due to the self-induced velocity observed for the shear layer with low A_R. However, the present results have confirmed that the vortex formation by this mechanism is also promoted by perturbations with $\Lambda/\delta \approx 12$.

4. The response of small-scale shear layers to velocity perturbations in turbulence

Turbulence contains many small-scale shear layers with a finite aspect ratio that are subject to a biaxial strain. Therefore, the wavelength dependence of the perturbed isolated

shear layer may be relevant to the evolution of shear layers in turbulence. Here, DNS is carried out for decaying turbulence to investigate the response of small-scale shear layers to velocity fluctuations with the efficient wavelength to promote shear instability. The results in § 3 suggest that the vortex formation from small-scale shear layers is promoted when they are subject to perturbations with $\Lambda/\delta \approx 12$ ($\Lambda/\delta_S \approx 7.2$). The visualisations of shear layers in turbulence indicate that the aspect ratio A_R is different for each shear layer (Nagata *et al.* 2020; Fiscaletti *et al.* 2021; Hayashi *et al.* 2021*a*). However, the rapid growth of spanwise vorticity by perturbations with $\Lambda/\delta \approx 12$ is observed for both large and small A_R in § 3. Furthermore, the p.d.f. of the layer thickness has a peak at $\delta_S \approx 4\eta$. Therefore, perturbations with a wavelength determined with $\delta_S \approx 4\eta$ and $\Lambda/\delta \approx 12$ ($\Lambda/\delta_S \approx 7.2$) are expected to affect the development of many shear layers in turbulence. This hypothesis is examined by simulating decaying turbulence initialised with an artificially modified velocity field of isotropic turbulence. Here, velocity fluctuations with the unstable wavelength for shear layers with a thickness of about 4η are artificially amplified or damped in isotropic turbulence. The response of shear layers to velocity fluctuations with a certain length scale is examined by comparing decaying turbulence initialised by the modified and original velocity profiles of isotropic turbulence.

4.1. *Decaying turbulence with artificial velocity perturbations*

DNS of decaying turbulence with artificial velocity perturbations is carried out to investigate the effects of external perturbations on the shear layers. The boundary conditions are the same as in the DNS of isotropic turbulence in § 2. The governing equations are (2.1) and (2.2) without external forcing, namely $f_i = 0$. Non-dimensionalisation considered in § 3 is not adapted for DNS of isotropic turbulence, and appropriate normalisation is applied when the results are presented. The DNS code is also the same as in § 2. The initial velocity field is generated by superimposing solenoidal velocity perturbations $\boldsymbol{u}_P(x, y, z)$ on an instantaneous flow field $\boldsymbol{u}_{HIT}(x, y, z)$ of forced homogeneous isotropic turbulence. Two types of perturbations are tested here. One is defined in a deterministic way with a sinusoidal function whereas another is given by a random velocity field with a prescribed energy spectrum. Both velocity fields are divergence-free and are characterised by a single length scale. For the sinusoidal velocity perturbations, $\boldsymbol{u}_P(x, y, z)$ is given by

$$\boldsymbol{u}_P(x, y, z) = \left(u_f \sin(2\pi y/\lambda_f), u_f \sin(2\pi z/\lambda_f), u_f \sin(2\pi x/\lambda_f)\right), \tag{4.1}$$

where the amplitude u_f and wavelength λ_f are the computational parameters. As the velocity and length scales of small-scale shear layers in turbulence are characterised by the Kolmogorov scales, u_f and λ_f are determined in terms of u_η and η.

Random velocity perturbations are generated by applying the inverse Fourier transform to velocity vectors in wavenumber space, $\hat{\boldsymbol{u}}_P(k_x, k_y, k_z)$, whose three-dimensional energy spectrum $E(k)$ is given by a Gaussian function as

$$E(k) = A_E \exp\left[-\frac{(\log k - \log k_p)^2}{2\delta_E^2}\right], \tag{4.2}$$

with $k = \sqrt{k_x^2 + k_y^2 + k_z^2}$. The spectrum has a peak at $k = k_p = 2\pi/\lambda_f$ whereas the width of the distribution is $\delta_E = C_\eta \log k_\eta$ with $k_\eta = 2\pi/\eta$ and $C_\eta = 0.005$. With two uniform random numbers that determine the phases, $\hat{\boldsymbol{u}}_P(k_x, k_y, k_z)$ can be calculated with (4.2) and the divergence-free condition in the wavenumber space following Johnsen *et al.* (2010).

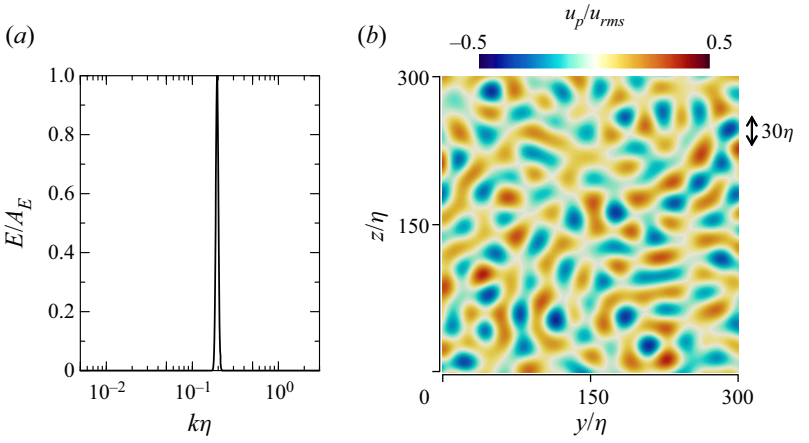

Figure 15. Random velocity perturbations used for the initial condition of D3L30R: (*a*) the energy spectrum $E(k)$ and (*b*) velocity in the x direction, u_P, with $\lambda_f/\eta \approx 30$. In (*a*), $E(k)$ is normalised for the peak to be 1.

Case	$\boldsymbol{u}_{HIT}$	$\boldsymbol{u}_P$	Re_λ	N^3	N_S	u_f/u_η	λ_f/η	$\Delta u_{rms}/u_{rms0}$
D1	NS1	—	43	256^3	10	0	—	—
D1L30	NS1	Sin	43	256^3	10	1.0	30.7	2.4 %
D1L30u1	NS1	Sin	43	256^3	10	1.2	30.7	3.5 %
D1L30u2	NS1	Sin	43	256^3	10	1.4	30.7	4.7 %
D1L30R	NS1	Random	43	256^3	10	—	30.7	2.4 %
D1L70	NS1	Sin	43	256^3	10	1.0	71.7	2.4 %
D2	NS2	—	72	512^3	5	0	—	—
D2L30	NS2	Sin	72	512^3	5	1.0	32.4	1.4 %
D3	NS3	—	128	1024^3	3	0	—	—
D3L30	NS3	Sin	128	1024^3	3	1.0	32.4	0.66 %
D3L30R	NS3	Random	128	1024^3	3	—	32.4	0.66 %

Table 3. Parameters of DNS of decaying turbulence with and without initial perturbations: the turbulent Reynolds number Re_λ of the original isotropic turbulence used for the initial condition, the number of grid points N^3, the number of simulations repeated for ensemble averages, N_S, the amplitude u_f and wavelength λ_f of the perturbations and the increase in r.m.s. velocity fluctuations due to the perturbations normalised by r.m.s. velocity fluctuations of the original isotropic turbulence, $\Delta u_{rms}/u_{rms0}$.

Then, the inverse Fourier transform of $\hat{\boldsymbol{u}}_P(k_x, k_y, k_z)$ yields $\boldsymbol{u}_P(x, y, z)$. The solenoidal velocity vector generated in this method has random phases in the wavenumber space and the energy spectrum with a single peak for $k_p = 2\pi/\lambda_f$. The constant A_E is determined such that the increment of r.m.s. velocity fluctuations due to the perturbations is equal to Δu_{rms}, which is a parameter of the simulation. Figure 15 shows $E(k)$ and u_P used in one of the simulations with $\lambda_f/\eta = 30$. A large peak appears at a wavenumber of k_p. The length corresponding to k_p characterises the profile of u_P, which does not have coherent patterns because of the random phases.

Table 3 summarises the parameters of DNS. For statistical analyses, DNS for each case is repeated N_S times with different initial velocity profiles of $\boldsymbol{u}_{HIT}$, which are obtained from different time instances of statistically steady homogeneous isotropic turbulence. Here, N_S is larger for a lower Reynolds number because the number of small-scale structures

contained in the computational domain decreases as the Reynolds number becomes small and more simulations have to be carried out for statistical convergence (Hayashi *et al.* 2021*a*). The perturbations are generated with sinusoidal functions (4.1) for 'Sin' and random velocity for 'Random'. The results of NS1, NS2 and NS3 in § 2 are used as the initial conditions. Therefore, the computational domain size and the number of grid points N^3 in the DNS of decaying turbulence are the same as those for the statistically steady isotropic turbulence. The table also includes the initial turbulent Reynolds number Re_λ. Cases D1, D2 and D3 consider decaying turbulence without perturbations, namely $u_f = 0$. Cases DnLm apply sinusoidal perturbations with $\lambda_f/\eta \approx m$ to the velocity profile taken from NSn whereas cases DnLmR adapt random velocity perturbations. As the periodic boundary conditions are applied in the DNS, λ_f is chosen such that $\boldsymbol{u}_P$ of (4.1) also satisfies the periodic boundary conditions. DNS is performed for $\lambda_f/\eta \approx 30$ and 70, which are determined with the shear layer thickness examined in § 2 and the wavenumber dependence of the isolated shear layer in § 3 as explained below. In each of the N_S simulations, the initial value of η is slightly different because different instances of isotropic turbulence are used in the initialisation. Therefore, the average of λ_f/η taken for N_S simulations is listed in table 3 whereas the r.m.s. fluctuations of λ_f/η among N_S simulations are less than 1 % of the averages. For all Reynolds numbers, $u_f/u_\eta = 0$ or 1.0 is assumed for the initial perturbations. In addition, the simulations are also performed with $u_f/u_\eta = 1.2$ and 1.4 (cases D1L30u1 and D1L30u2) for the series of D1, which examine the influence of the perturbation amplitude. For random velocity in DnLmR, A_E in (4.2) is determined for $\Delta u_{rms}/u_{rms0}$ to match the corresponding cases with sinusoidal perturbations, DnLm. The unperturbed and perturbed cases, Dn and DnL30, are compared for each Reynolds number. Time is advanced until $t = 15\tau_{\eta 0}$, where $\tau_{\eta 0}$ is the Kolmogorov time scale at $t = 0$.

The parameters of the perturbations are compared with the characteristics of shear layers in § 2 and the isolated shear layer in § 3. For isotropic turbulence, the typical thickness of shear layers is $\delta_S/\eta \approx 4$, which is estimated from the peak of the joint p.d.f. in figure 5(*a*). The numerical simulations in § 3 suggest that the vortex formation is effectively promoted by perturbations with a wavelength of $\Lambda/\delta \approx 12$, which is equivalent to $\Lambda/\delta_S \approx 7.2$ because of $\delta_S/\delta = 1.67$. Thus, $\Lambda/\delta \approx 12$ corresponds to $\Lambda/\eta = (\Lambda/\delta_S)(\delta_S/\eta) \approx 29$ for small-scale shear layers in isotropic turbulence. The wavelength of the perturbations is close to $\Lambda/\eta \approx 29$ in cases DnL30, for which the perturbations are expected to have significant influences on the evolution of the shear layers. In addition, case D1L70 considers the perturbations with $\Lambda/\eta = 71.7$, which corresponds to $\Lambda/\delta \approx 30$. The results in § 3 suggest that the perturbations with this wavelength are not as conducive to the vortex formation as those with $\Lambda/\eta \approx 30$ ($\Lambda/\delta \approx 12$).

The typical velocity jump across the shear layers in turbulence is about $u_S/u_\eta = 5$, which is estimated from the joint p.d.f. in figure 5(*b*). The velocity jump u_S is related to the reference velocity scale u_r used in the simulations of the isolated shear layer by $u_S/u_r \approx 0.9$. Thus, $u_f/u_\eta = 1$, 1.2 and 1.4 used for the perturbations of decaying turbulence are equivalent to $u_f/u_r = 0.18$, 0.22 and 0.25, respectively. These amplitudes are larger than those considered for the isolated shear layer in § 3, and the perturbations are expected to be strong enough to affect the shear layer development in turbulence. The artificial velocity fluctuations affect the initial r.m.s. velocity fluctuations. The increase of the r.m.s. velocity fluctuations, Δu_{rms}, normalised by the original r.m.s. velocity fluctuations of isotropic turbulence, u_{rms0}, is also listed in table 3. For all cases, $\Delta u_{rms}/u_{rms0}$ is smaller than 5 %. Because the amplitude of perturbations is determined with the Kolmogorov velocity

scale, $\Delta u_{rms}/u_{rms0}$ decreases with the Reynolds number. For the highest Re case, D3L30, $\Delta u_{rms}/u_{rms0}$ is less than 1 %. These small values confirm that the perturbations are much weaker than the velocity fluctuations of isotropic turbulence.

The perturbations with a length of λ_f cause a spike in an energy spectrum. Turbulence with a spectral spike has also been considered in other studies. These studies mostly concern a fully developed state of turbulence with a spectral spike, whose effects are already felt throughout turbulent motions of all length scales. Yeung & Brasseur (1991) investigated turbulence generated by anisotropic vortical forcing, which also causes a spectral spike for a wavelength of forced vortices. Their analysis concerns fully developed turbulence generated by vortical forcing, by which large-scale anisotropy affects small-scale turbulent motions. Similar anisotropic turbulence with a spectral spike was also studied in Goto & Vassilicos (2016). Another example is a study of a turbulent mixing layer in Takamure *et al.* (2019), where large-scale coherent vortices cause spikes in the energy spectrum. They have shown the relevance of the spectral spikes to the non-equilibrium scaling of the energy dissipation rate. These studies have discussed the influences of spectral spikes on the statistics of turbulence. The perturbation response of small-scale shear layers in the present DNS can be interpreted as the transient regime of the interaction between the spectral spike and small-scale velocity fluctuations of isotropic turbulence, where the influence of the perturbations gradually prevails. In addition, the present study mainly discusses small-scale vortices and shear layers, which are usually difficult to identify in wavenumber space. However, the influence of the perturbations observed for shear layers in physical space should affect the flow evolution in wavenumber space, and the insight from the present analysis can be useful for future studies of the scale-by-scale analysis in wavenumber space.

4.2. *Decaying turbulence initialised with a band-cut filtered velocity field*

Fluid motions with the efficient wavelength to promote small-scale shear instability also exist in turbulence because this length, namely about 30η, is greater than the Kolmogorov scale. The role of velocity fluctuations of turbulence in the shear layer development is also investigated with DNS of decaying turbulence. Although the interaction between turbulent motions with a length scale of about 30η and small-scale shear layers may be understood as the interaction of different scales studied with Fourier analysis, it is difficult to explicitly examine the influence of velocity fluctuations at a particular length scale on the shear layers because the shear layers cannot be identified in wavenumber space. Therefore, the present study takes an alternative approach to examine the response of shear layers to velocity fluctuations of turbulence. The DNS of decaying turbulence is initialised with a velocity field which is obtained by applying a band-cut filter to a three-dimensional velocity field of isotropic turbulence. The filter damps velocity fluctuations of a certain length scale. Then, flow evolution is compared for the initial conditions given by the filtered and original velocity profiles to determine whether or not the velocity fluctuations damped by the filter are important in the shear layer development. A similar approach was used in Cimbala, Nagib & Roshko (1988), Jiménez & Moin (1991) and Jiménez (2018), where large-scale turbulent structures or vorticity fluctuations within a region of interest were artificially damped or eliminated to examine their influences on flow evolution.

Following Leung, Swaminathan & Davidson (2012) and Doan, Swaminathan & Chakraborty (2017), the filter is applied in wavenumber space. First, the three-dimensional Fourier transform is applied to the velocity field of isotropic turbulence to obtain the velocity vector in the wavenumber space, $\hat{\boldsymbol{u}}(k_x, k_y, k_z)$. Then, $\hat{\boldsymbol{u}}$ is multiplied by the

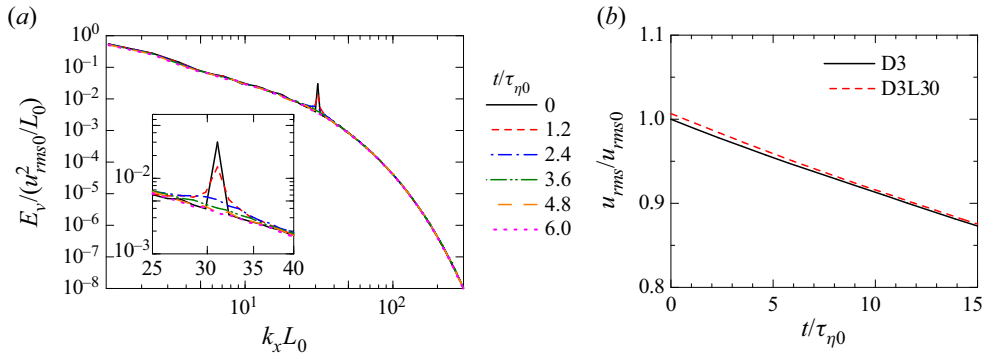

Figure 16. (*a*) Energy spectrum of v, E_v, calculated for the wavenumber in the x direction, k_x, in D3L30. (*b*) The decay of r.m.s. velocity fluctuations u_{rms} in D3 and D3L30. The results are non-dimensionalised with the r.m.s. velocity fluctuations u_{rms0}, integral scale L_0 and the Kolmogorov time scale $\tau_{\eta0}$ of statistically stationary homogeneous isotropic turbulence used for the initial condition.

following band-cut filter $T(k)$ defined with $k = \sqrt{k_x^2 + k_y^2 + k_z^2}$:

$$T(k) = 1 - \exp\left[-\frac{(\log k - \log k_p)^2}{2\delta_E^2}\right]. \tag{4.3}$$

This function is similar to the energy spectrum in (4.2), and $T(k) \approx 0$ for $k \approx k_p$ and $T(k) = 1$ otherwise. Then, the band-cut filtered velocity field is obtained by the inverse Fourier transform applied to $T\hat{\boldsymbol{u}}$ and is used as an initial condition of DNS of decaying turbulence. The wavelength k_p is determined as $k_p = 2\pi/\lambda_f$ while δ_E is $\delta_E = C_\eta \log k_\eta$ with $C_\eta = 0.005$, as also assumed for the perturbations given by (4.2). The filter damps velocity fluctuations with a length scale of λ_f. We have also tested different filters, such as a band-cut filter defined with a top-hat band-pass filter in Fourier space (Cao, Chen & Doolen 1999; Baerenzung *et al.* 2010; Goto, Saito & Kawahara 2017; Hirota *et al.* 2017), and have confirmed that the results are not sensitive to the choice of filters.

Filtered velocity fields for the initial condition are prepared with the results of NS3. The same snapshots of NS3 have been used in D3, D3L30 and D3L30R presented above. The cutoff wavelength of the filter, $k_p = 2\pi/\lambda_f$ in (4.3), is given by $\lambda_f = 30\eta$ or 140η. The filter with $\lambda_f = 140\eta$ damps large-scale velocity fluctuations because 140η corresponds to 0.6 times the integral scale. On the other hand, velocity fluctuations of the unstable wavelength for shear layers are damped by the filter with $\lambda_f = 30\eta$. Cases with the filters of $\lambda_f = 30\eta$ and 140η are referred to as D3L30F and D3L140F, respectively. Computational parameters other than the initial conditions are the same as in D3. The results are compared for D3, D3L30F and D3L140F to reveal the role of the filtered velocity component in the shear layer development.

4.3. *Results and discussion*

The results of DNS with artificial perturbations in § 4.1 are presented first whereas the role of internal velocity fluctuations in turbulence is discussed later. Figure 16(*a*) shows the temporal evolution of a one-dimensional energy spectrum of v, E_v, for a wavenumber in the x direction, k_x, in D3L30. The results are shown from $t/\tau_{\eta0} = 0$ to 6. The initial perturbations for v are given in a form of $\sin(x)$, which contributes to the peak in $E_v(k_x)$. This peak decays with time and is no longer identified after $t/\tau_{\eta0} = 4.8$. As the

perturbations added to the initial field is weak, it hardly influences the overall spectral shape. Figure 16(*b*) presents a comparison between D3 and D3L30 for the decay of r.m.s. velocity fluctuations normalised by the value of isotropic turbulence. At $t = 0$, the perturbations in D3L30 cause u_{rms} to increase by about 0.6 % compared with the unperturbed case (D3). This increase is not large enough to significantly alter the decay rate of u_{rms}. However, u_{rms} in D3L30 seems to gradually approach that in D3, implying a larger energy dissipation rate in D3L30.

The number of vortices (vortex tubes) is compared for decaying turbulence with and without initial perturbations. As also done in previous studies (Jiménez & Wray 1998), the vortices are detected by thresholding a quantity related to rotating motion. The intensity of rotating motion I_R defined with the triple decomposition of a velocity gradient tensor is used in the vortex identification in this study. The vortices identified with I_R are visualised in figure 1 for isotropic turbulence while those in other flows, such as wakes, jets and boundary layers, can be found in Kolář & Šístek (2014) and Hayashi *et al.* (2021*a*). Vortices in turbulence can also be detected with so-called Q and λ_2 criteria (Chong, Perry & Cantwell 1990; Jeong & Hussain 1995). Vortices identified with I_R were compared with those with Q and λ_2 criteria in Šístek *et al.* (2012) and Kolář & Šístek (2014), where the difference among these identification methods was shown to be small for various flows, such as a transitional boundary layer and a turbulent wake of a flat plate. This is because positive Q is strongly correlated with I_R in turbulence (Nagata *et al.* 2020). The results presented in this paper do not change even if the vortices are identified with the Q criterion, as shown below.

The algorithm to identify vortices with I_R is the same as that used with enstrophy for various turbulent flows (Jiménez *et al.* 1993; Jiménez & Wray 1998; da Silva *et al.* 2011; Jahanbakhshi *et al.* 2015; Ghira *et al.* 2022) although the enstrophy is not used in this study because it cannot distinguish between vortex tubes and shear layers. The computational grid points that belong to vortices are identified with a given threshold I_{Rth} as points with $I_R > I_{Rth}$. Then, the connectivity of the vortex points is examined to define the vortices as connected points with $I_R > I_{Rth}$, which belong to the same vortex. Then, the number of points belonging to each vortex is counted. Following Jiménez & Wray (1998) and da Silva *et al.* (2011), the vortices for which less than 30 points are assigned are discarded from the subsequent analysis because these vortices have I_R close to the threshold and appear as noise-like patterns rather than coherent structures. Finally, the number of vortices detected with I_R, N_{I_R}, is counted. As each simulation is repeated N_S times, N_{I_R} is averaged for N_S simulations.

The number of detected vortices N_{I_R} depends on the choice of the threshold I_{Rth}. Instead of using a specific threshold, N_{I_R} is evaluated for a wide range of I_{Rth}. Figure 17 plots N_{I_R} with the normalised threshold $I_{Rth}/\langle I_R\rangle$ at $t/\tau_{\eta 0} = 0$, 2 and 6 for D1, D1L30 and D1L70. Here, $\langle I_R\rangle$ is used for normalisation because $\langle I_R\rangle$ decreases with time and becomes large with the Reynolds number. Except for very small $I_{Rth}/\langle I_R\rangle$, N_{I_R} decreases with an increase of $I_{Rth}/\langle I_R\rangle$ because the vortices with moderately large I_R are not identified with a large threshold. However, N_{I_R} also decreases as $I_{Rth}/\langle I_R\rangle$ becomes small for $I_{Rth}/\langle I_R\rangle \lesssim 1.5$. Vortex regions identified with a very small threshold are connected even if these regions belong to different vortices. Therefore, the threshold should be chosen from the range where N_{I_R} decreases with increasing I_{Rth}, namely $I_{Rth}/\langle I_R\rangle \gtrsim 1.5$, for which the effects of the initial perturbations are discussed by comparing D1 with D1L30 and D1L70. At $t = 0$ in figure 17(*a*), N_{I_R} hardly differs for the three cases, and the perturbations do not alter the initial distribution of vortices. However, a difference in N_{I_R} between D1L30 and the others becomes clearer with time. For all thresholds, N_{I_R} for D1L30 is larger than those for D1 and D1L70 at $t/\tau_{\eta 0} = 2$ and 6, and more vortices are found in the flow when the initial

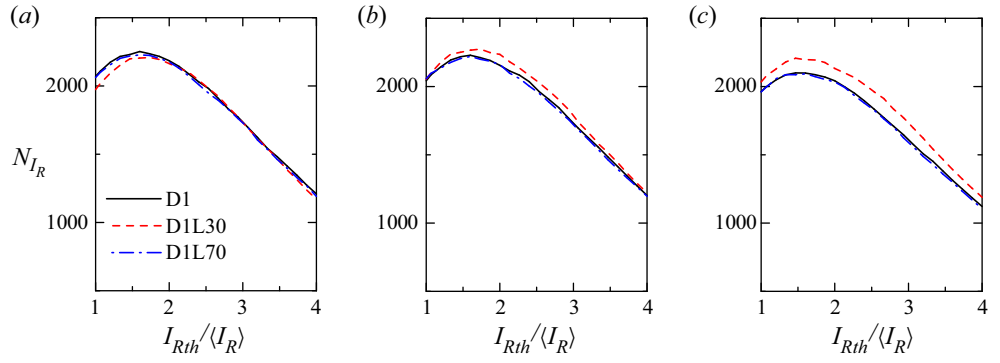

Figure 17. Threshold dependence of the number of vortices, N_{I_R}, in D1, D1L30 and D1L70 at (*a*) $t = 0$, (*b*) $t/\tau_{\eta 0} = 2$ and (*c*) $t/\tau_{\eta 0} = 6$. The vortices are detected by the intensity of rotating motion I_R with a threshold I_{Rth}. N_{I_R} is plotted as a function of I_{Rth} normalised by the average of I_R, $\langle I_R\rangle$.

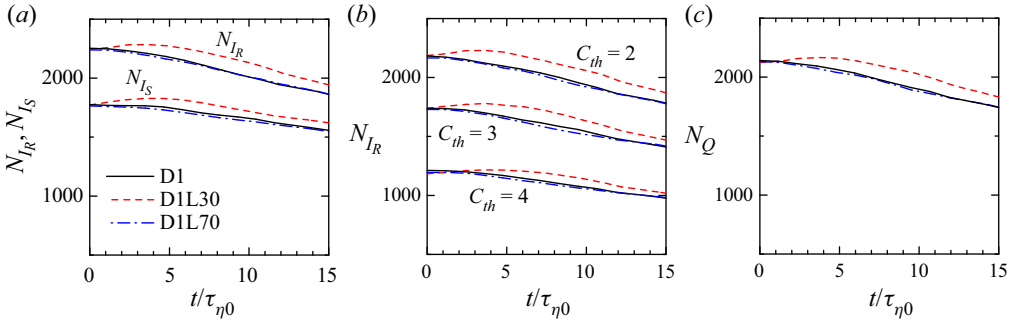

Figure 18. Temporal variations of the number of detected vortices N_{I_R} in D1, D1L30 and D1L70. The vortices are detected with the intensity of rotating motion I_R with (*a*) the threshold that yields the maximum number of vortices at each time step and (*b*) those determined with the average of I_R as $C_{th}\langle I_R\rangle$ with $C_{th} = 2$, 3 and 4 whereas the results obtained with the Q criterion are presented in (*c*), where the threshold is determined such that the number of detected vortices is the maximum at each time step. Panel (*a*) also presents the number of shear layers, N_{I_S}, detected with I_S, for which the threshold is determined based on the threshold dependence of N_{I_S}.

velocity profile is perturbed by velocity fluctuations with $\lambda_f/\eta \approx 30$. The perturbations are also added in D1L70, and the increase of initial u_{rms} caused by the perturbations is the same for D1L30 and D1L70. However, the increase in the number of vortices due to the perturbations does not occur for D1L70. These results are qualitatively the same for all thresholds.

The temporal variations of N_{I_R} are examined with several thresholds for D1, D1L30 and D1L70. As the threshold increases, N_{I_R} decreases because the vortices with moderately strong rotation are disregarded for a large threshold. However, as discussed above, a very small threshold results in a decrease of N_{I_R} because multiple vortices are identified as one large structure. These tendencies suggest that the threshold corresponding to the maximum N_{I_R} is appropriate to detect vortices with both large and small I_R without the problem of vortex connection caused by a small threshold. For this case, the threshold value normalised by $\langle I_R\rangle$ also varies with time. Figure 18(*a*) plots the temporal variations of N_{I_R} calculated with the threshold corresponding to the maximum N_{I_R}. When the perturbations

are not added to the initial velocity field (D1), N_{I_R} monotonically decreases with time. However, N_{I_R} increases until $t/\tau_{\eta 0} \approx 4$ in D1L30, for which more vortices exist in the flow compared with the unperturbed case. This influence of the perturbations is observed only for D1L30, where the perturbation wavelength matches the anticipated unstable wavelength of typical small-scale shear layers. When the perturbations have a wavelength of $\lambda_f/\eta \approx 70$ (D1L70), the temporal variation of N_{I_R} hardly differs from the unperturbed case (D1) even though the perturbations imposed in D1L30 and D1L70 have the same turbulent kinetic energy as confirmed from the same value of $\Delta u_{rms}/u_{rms0}$ in table 3.

Shear layers can be detected with the same method used for vortices by using I_S instead of I_R. The threshold I_{Sth} is also determined by the same method as I_{Rth} based on the I_{Sth} dependence of the number of detected shear layers. Figure 18(*a*) shows the number of shear layers, N_{I_S}, for the three simulations. Both N_{I_S} and N_{I_R} in D1L30 are larger than those in D1 and D1L70, and the perturbations in D1L30 result in the increase of both vortices and shear layers. The kinetic energy budget around shear layers suggests that the energetic flow that contributes to the shear is generated and sustained by vortices (Watanabe & Nagata 2022). Furthermore, when the roll-up of a shear layer occurs, it splits into more than one shear layer around the generated vortex (Corcos & Lin 1984). Therefore, more shear layers appear when the number of vortices is increased by the influence of perturbations.

Figure 18(*b*) presents N_{I_R} obtained with the threshold determined with the average of I_R as $I_{Rth} = C_{th}\langle I_R\rangle$. The temporal variations of N_{I_R} in D1, D1L30 and D1L70 are compared for three thresholds of $C_{th} = 2$, 3 and 4. Although N_{I_R} varies with C_{th}, the temporal variations of N_{I_R} are qualitatively similar for all C_{th}. Therefore, the increase in the number of vortices due to the perturbations in D1L30 can be observed regardless of the threshold. Finally, the effects of the perturbations are also examined for the vortices detected with the second invariant of $\nabla \boldsymbol{u}$, $Q = (\Omega_{ij}\Omega_{ij} - S_{ij}S_{ij})/2$, for which the region of $Q > Q_{th}$ is identified as vortices. Here, Q_{th} is determined such that the number of detected vortices, N_Q, is the maximum. Figure 18(*c*) plots N_Q with time. As also found for the vortices identified with I_R, more vortices appear in D1L30 whereas the number of vortices is not influenced by the perturbations in D1L70. These results confirm that the increase in the number of vortices in D1L30 is a physically meaningful result and is not an artefact due to the vortex identification methods.

Figure 19 visualises the evolution of one of the shear layers. The shear layers (white) and vortices (orange) are visualised with the isosurfaces of I_S and I_R, respectively. Figures 19(*a–d*) and 19(*e–h*) show the results of D1 and D1L30, respectively. A large shear layer is observed at $t = 0$ in both cases (figure 19*a*,*e*). As this shear layer evolves with time, vortex A appears in D1L30 in figure 19(*g*). The shear layer which generates vortex A is disappearing in figure 19(*h*). However, this shear layer keeps its flat shape for a long time in D1, where no perturbations are added to the initial velocity. In figure 19(*d*,*h*), vortex B also fully develops from the shear layer in D1L30 whereas this vortex is still developing in the shear layer in D1. A comparison between figures 19(*c*,*d*) and 19(*g*,*h*) suggests that the lifetime of the shear layers is shortened by the perturbations. The vortex formation from the shear layers naturally occurs in turbulence (Vincent & Meneguzzi 1994; Passot *et al.* 1995; Watanabe *et al.* 2020). This process visualised in Watanabe *et al.* (2020) looks similar to the evolution of the shear layers and vortices in figure 19(*e–h*). Therefore, the perturbations in D1L30 do not directly destroy the shear layers at $t = 0$ but promote the vortex formation from the shear layers.

Figure 20(*a*) shows the variations of the number of vortices identified with I_R for D2, D3, D2L30 and D3L30. Here, the threshold is determined as $I_{Rth} = C_{th}\langle I_R\rangle$ with $C_{th} = 3$. Because the vortices are small-scale structures characterised by the Kolmogorov scale,

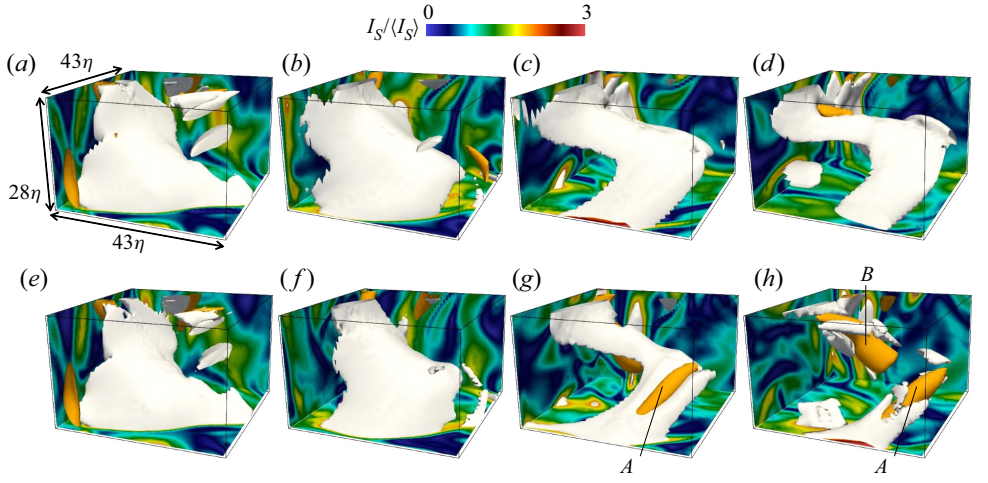

Figure 19. Temporal evolutions of shear layers and vortices, which are visualised with the isosurfaces of $I_S/\langle I_S\rangle = 2$ (white) and $I_R/\langle I_R\rangle = 6$ (orange), respectively. The colour contour of I_S is shown on the surface of the visualised domain. (*a–d*) Unperturbed case D1 and (*e–h*) perturbed case D1L30. Time increases from left to right as (*a,e*) $t/\tau_{\eta 0} = 0$, (*b,f*) $t/\tau_{\eta 0} = 2$, (*c,g*) $t/\tau_{\eta 0} = 4$ and (*d,h*) $t/\tau_{\eta 0} = 6$.

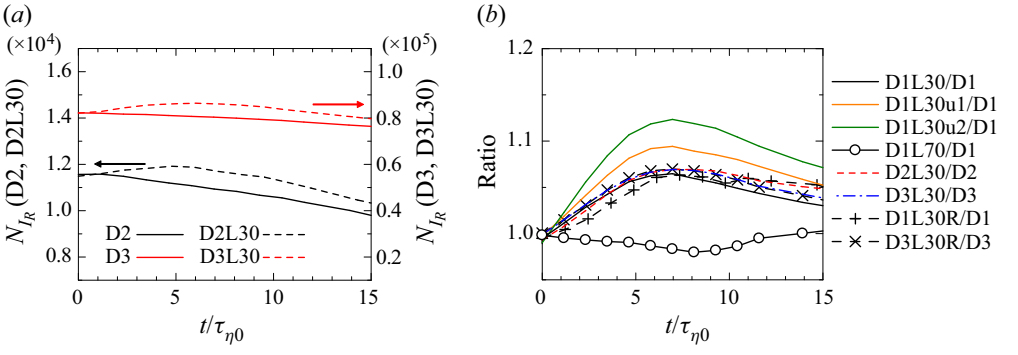

Figure 20. Temporal variations of (*a*) the number of vortices, N_{I_R}, in D2, D2L30, D3 and D3L30 and (*b*) a ratio of N_{I_R} between the perturbed and unperturbed cases.

which becomes small with increasing Re_λ, N_{I_R} increases from D1 to D3. However, the effect of the initial perturbations is similar for all Reynolds numbers, and N_{I_R} in the perturbed cases with $\lambda_f/\eta \approx 30$ becomes large compared with the unperturbed cases.

Figure 20(*b*) shows the variations of the ratio of N_{I_R} between the perturbed and unperturbed cases. The results for sinusoidal and random perturbations are also compared in the figure. For both perturbations, the ratio exceeds 1 for $\lambda_f/\eta \approx 30$ (D*n*L30 and D*n*L30R), and the increase in the number of vortices is observed for this wavelength regardless of the Reynolds number and the types of perturbations. Because the shear layers are located almost randomly in the flow, the relative positions of the shear layers to the peak of sinusoidal perturbations are not constant. Therefore, the effects of sinusoidal perturbations are similar to those of random velocity perturbations. As the number of vortices increases, the ratio reaches a peak at $t/\tau_{\eta 0} \approx 7$ and then decays with time. The time corresponding to the peak hardly depends on the Reynolds number when the Kolmogorov time scale is used for normalisation. Therefore, how the perturbations

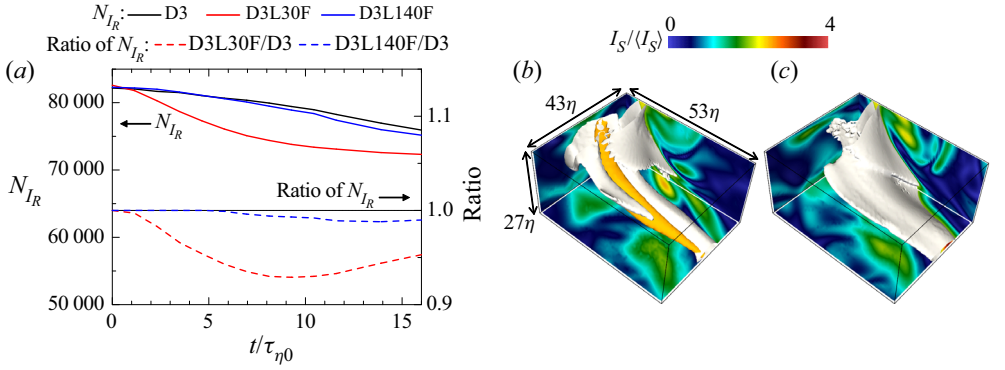

Figure 21. (*a*) The number of vortices N_{I_R} in decaying turbulence initialised with a band-cut filtered velocity field and an original velocity field of isotropic turbulence. The ratio of N_{I_R} between the filtered and original cases is also shown for comparison. The vortices are detected as regions of $I_R \geqslant C_{th}\langle I_R\rangle$ with $C_{th} = 3$, where $\langle I_R\rangle$ is evaluated with D3. Visualisation of shear layers (white) and vortices (orange) at $t/\tau_{\eta 0} = 6$ in (*b*) D3 and (*c*) D3L30F. The isosurface values are the same as in figure 19.

affect the shear layers is a small-scale process whose time scale is characterised by the Kolmogorov time scale. Visualisation of the temporal evolution of small-scale shear layers in isotropic turbulence has shown that the natural roll-up of the shear layer is also completed within about five times the Kolmogorov time scale (Watanabe *et al.* 2020). This time scale of the roll-up is close to $t/\tau_{\eta 0} \approx 7$, at which the ratio of N_{I_R} reaches the peak in figure 20(*b*). The peak value at $t/\tau_{\eta 0} \approx 7$ is about 1.07 for D1L30, D2L30 and D3L30 despite the difference in the Reynolds number. For these cases, the amplitude of perturbations, u_f, is determined based on the Kolmogorov velocity scale u_η as $1.0u_\eta$ whereas u_η/u_{rms} decreases with the Reynolds number. Therefore, the increment in the number of vortices for a given wavelength depends on u_f/u_η. Because u_η decreases with the Reynolds number, less turbulent kinetic energy is required for the perturbations to cause an increase in the number of vortices at a higher Reynolds number. A comparison among the series of D1 suggests that N_{I_R} increases as u_f/u_η becomes large. For $u_f/u_\eta = 1.4$ in D1L30u2, N_{I_R} increases by more than 10 % from the unperturbed case. The increase in the number of vortices does not occur in D1L70, for which the ratio stays around 1. These results are consistent with the response of the isolated shear layer to perturbations in § 3: the vortex formation rapidly occurs with the perturbations with $\lambda_f/\eta \approx 30$ estimated with $\lambda_f/\delta_S \approx 7.2$ and $\delta_S/\eta \approx 4$ while those with a larger wavelength are not efficient in promoting the vortex formation.

The above results have shown that the external perturbations with a wavelength of 30η promote the vortex formation from shear layers. The results for decaying turbulence initialised with a filtered velocity field explained in § 4.2 are presented to examine whether the shear instability in turbulence is promoted by internal velocity fluctuations with this wavelength. Figure 21 compares the variations of the number of vortices N_{I_R} for D3, D3L30F and D3L140F, together with the ratio of N_{I_R} between the filtered and original cases. The initial velocity fields of D3L30F and D3L140F do not contain velocity fluctuations with wavelengths of 30η and 140η, respectively. A comparison of three cases shows that N_{I_R} in D3L30F is smaller than those in the other cases, suggesting that fewer vortices are generated by the shear instability when the velocity fluctuations with a length of 30η are damped by the filter. The reduction of N_{I_R} is not significant in D3L140F. Figures 21(*b*) and 21(*c*) visualise one of the shear layers and nearby vortices in D3 and D3L30F, respectively. Both figures visualise the same region of the computational domain

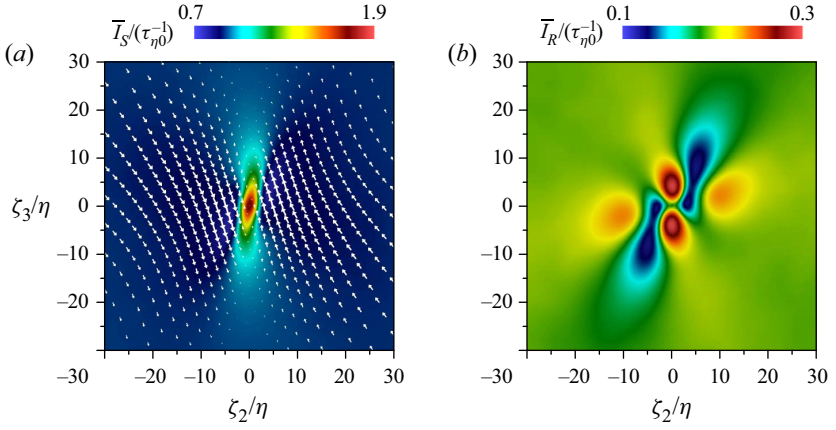

Figure 22. A mean flow field around shear layers in the initial velocity field of D3L30F, which is generated by applying the band-cut filter with the cutoff length of $\lambda_f = 30\eta$ to isotropic turbulence. (*a*) Mean shear intensity $\overline{I_S}$ and mean velocity vectors and (*b*) mean intensity of rotating motion $\overline{I_R}$ on the ζ_2–ζ_3 plane at the centre of shear layers ($\zeta_1 = 0$).

at $t/\tau_{\eta 0} = 6$, at which the reduction of the number of vortices is observed in D3L30F. The shear layer in figure 21(*b*) is being broken and a vortex has been generated at the centre of the shear layer. This shear layer has a flat shape in D3L30F without generating the vortex. Thus, the shear layer can survive a long time when the velocity fluctuations with 30η are damped in the initial field. These results confirm that turbulent motions with a length of 30η play a dynamically important role in vortex formation by small-scale shear instability.

The flow field around shear layers in the initial filtered velocity field of D3L30F is investigated by taking conditional averages around the shear layers. For each shear layer detected by the method described in § 2, variables on the DNS grid are interpolated on the shear coordinate $(\zeta_1, \zeta_2, \zeta_3)$. Then, the ensemble averages of many shear layers are calculated as functions of $(\zeta_1, \zeta_2, \zeta_3)$. This average is denoted by an overline, e.g. $\overline{I_S}$. Figure 22 shows the mean intensities of shear and rotation, $\overline{I_S}$ and $\overline{I_R}$, around the shear layers in the initial field of D3L30F. The averages are shown on the ζ_2–ζ_3 plane at $\zeta_1 = 0$. Figure 22(*a*) also shows the mean velocity vectors. The results for original isotropic turbulence were presented in Watanabe & Nagata (2022). The shear is associated with the mean flows in $\pm\zeta_3$ directions on the sides of the shear layer with large $\overline{I_S}$ centred at $(\zeta_2, \zeta_3) = (0, 0)$. In figure 22(*b*), four approximately circular regions with large $\overline{I_R}$ are found around $(\zeta_2, \zeta_3) = (0, 0)$. Two of them are located within the shear layer on $\zeta_2 = 0$ whereas the others appear on the sides of the shear layer. Similar rotating motions were also identified in the mean flow pattern in the strain eigenframe (Elsinga & Marusic 2010). The profiles of $\overline{I_S}$, $\overline{I_R}$ and mean velocity hardly differ from isotropic turbulence (Watanabe & Nagata 2022) even though the present results are obtained for the filtered velocity field, for which the instability of shear layers is inhibited. It is implied that rotating motions around the shear layers are not related to the velocity fluctuations which promote small-scale shear instability.

The effects of the increase or decrease in the number of vortices are examined for the kinetic energy dissipation rate $\varepsilon = 2\nu S_{ij}S_{ij}$. Figure 23(*a*) compares the temporal variation of the averaged dissipation rate $\langle\varepsilon\rangle$ for D3, D3L30 and D3L30F. The shear instability is promoted and inhibited in D3L30 and D3L30F, respectively. For $t/\tau_{\eta 0} \leq 10$, the dissipation rates in D3L30 and D3L30F are larger and smaller than that of the original

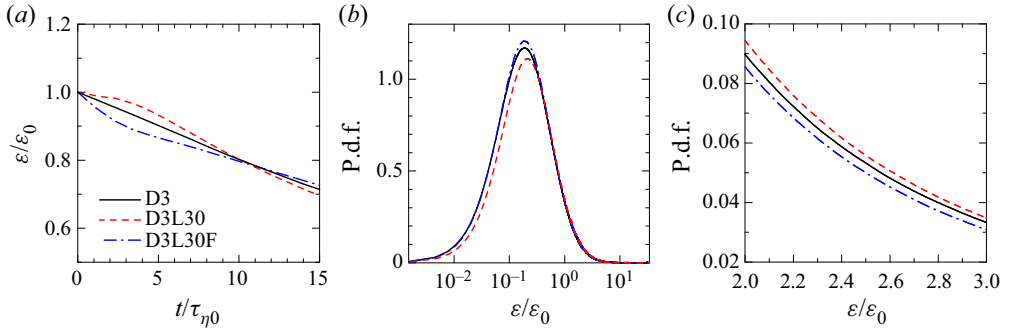

Figure 23. (*a*) Temporal variations of averaged kinetic energy dissipation rate $\langle\varepsilon\rangle$ normalised by the initial value ε_0 in D3, D3L30 and D3L30F. (*b*, *c*) Probability density function of ε at $t/\tau_{\eta 0} = 5$.

case, D3. Thus, when the initial velocity field is modified such that the shear instability is promoted, the dissipation rate also increases whereas the opposite effect is found when the instability is inhibited. The increase in the number of vortices results in more small-scale shear layers. Although for the local fluid motions considered in the triple decomposition, both shear and elongation contribute to the rate-of-strain tensor, the shear has a greater contribution to $S_{ij}S_{ij}$ than the elongation (Nagata *et al.* 2020). Therefore, a large dissipation rate in D3L30 can be explained by the increased number of shear layers. For $t/\tau_{\eta 0} \geqslant 10$, an opposite trend for $\langle\varepsilon\rangle$ is observed: $\langle\varepsilon\rangle$ for the perturbed and filtered cases is smaller and larger than that for the original case. The enhanced dissipation in the perturbed case results in a rapid decay of turbulent kinetic energy at small scales. Then, there is less kinetic energy to be dissipated at a late time when the perturbations are added, and therefore $\langle\varepsilon\rangle$ can be small. Figure 23(*b*,*c*) compare the p.d.f. of ε at $t/\tau_{\eta 0} = 5$ for the three cases. In figure 23(*b*), a logarithmic scale for ε is used to compare the probability distribution for small ε. The p.d.f. suggests that small ε is less frequently observed when the perturbations are added in D3L30. The peak of the p.d.f. for the filtered velocity in D3L30F is larger than that in D3, and the probability to observe small ε increases in D3L30F. The p.d.f. for relatively large ε is shown in figure 23(*c*). The probability to observe large ε increases and decreases when the velocity fluctuations with a length of 30η are added and damped, respectively.

Figure 24 shows the p.d.f. of the production rates of enstrophy and strain at $t/\tau_{\eta 0} = 5$ in D3, D3L30 and D3L30F. The enstrophy production and strain self-amplification are written as $P_\omega = \omega_i S_{ij}\omega_j$ and $P_S = -S_{ij}S_{jk}S_{ki}$, respectively. The overall distribution of the p.d.f. is similar for all cases. However, the profile becomes slightly wider and narrower for D3L30 and D3L30F, respectively, than for D3. The insets confirm that the p.d.f. for large P_ω and P_S increases when the shear instability is promoted by the perturbations whereas the opposite effect is found when the instability is inhibited. Consequently, the averages of P_ω and P_S increase by 20 % by the perturbations in D3L30 and decrease by 4 % by the filter in D3L30F. Shearing motions have dominant contributions to P_ω and P_S (Watanabe *et al.* 2020). The increases of $\langle P_\omega\rangle$ and $\langle P_S\rangle$ by the perturbations are also explained by the increased number of shear layers, which can be generated by vortices.

5. Conclusions

The response of small-scale shear layers to velocity perturbations has been studied with the analysis of shear layers in isotropic turbulence, numerical simulations of a

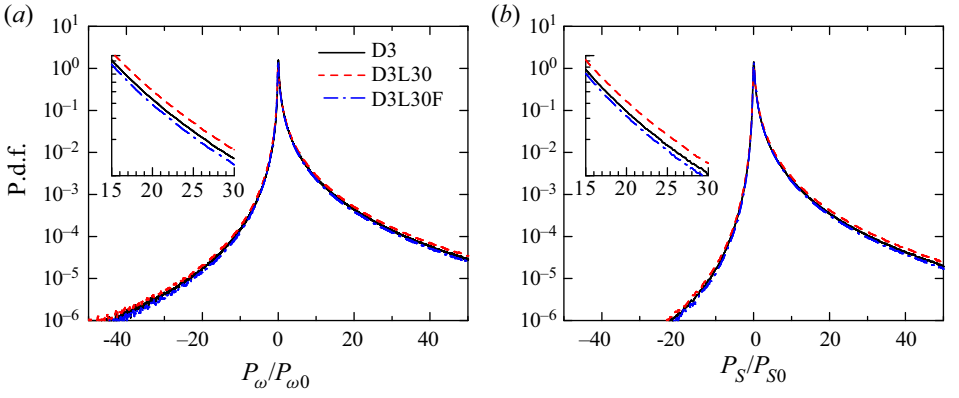

Figure 24. Probability density functions of (*a*) enstrophy production $P_\omega = \omega_i S_{ij} \omega_j$ and (*b*) strain self-amplification $P_S = -S_{ij} S_{jk} S_{ki}$ at $t/\tau_{\eta 0} = 5$ in D3, D3L30 and D3F30F. The production rates, P_ω and P_S, are normalised by their initial mean values denoted by $P_{\omega 0}$ and P_{S0}.

perturbed isolated shear layer in a biaxial strain field and DNS of decaying turbulence. As summarised below, vortex formation from the shear layers in turbulence is efficiently promoted by velocity fluctuations with a wavelength of approximately 30η, which is the most unstable wavelength for the instability of small-scale shear layers.

The thickness δ_S and velocity jump u_S of each shear layer have been examined with DNS of isotropic turbulence. The typical shear layers have $\delta_S/\eta \approx 4$ and $u_S/u_\eta \approx 5$ regardless of Re_λ. Many shear layers have the shear Reynolds number of $Re_S = \delta_S u_S/\nu \approx 20$ although Re_S ranges approximately from 10 to 70. Furthermore, the equilibrium relation between a strain rate and the layer thickness of Burgers' vortex layer is valid for most shear layers with $Re_S \approx 20$.

Numerical simulations have been carried out to investigate the development of an isolated shear layer with a finite aspect ratio A_R. The model considers a shear layer subject to a biaxial strain, which is observed in the mean flow field around shear layers in turbulence (Watanabe *et al.* 2020; Hayashi *et al.* 2021*a*). When the aspect ratio is small, the self-induced velocity of the shear layer causes the roll-up of the layer and generates a vortex. On the other hand, the shear layer with large A_R is simply distorted without vortex formation if no perturbations are added. Perturbations can trigger the vortex formation in the large-A_R shear layer, as also observed for a parallel shear flow with $A_R \to \infty$ in previous studies. For both cases of large and small A_R, the vortex formation is promoted by the perturbations whose wavelength Λ divided by the layer thickness δ_S is $\Lambda/\delta_S \approx 7$, where δ_S is the half-width of shear intensity. The perturbations with smaller or larger wavelengths are not efficient in promoting the instability and sometimes delay or inhibit the vortex formation.

Many small-scale shear layers in turbulence are expected to be significantly influenced by perturbations with a wavelength of about 30η, which is estimated from the typical thickness of small-scale shear layers in turbulence and the perturbation wavelength which is efficient in promoting vortex formation of the isolated shear layer. The response of turbulence to artificial velocity perturbations has been investigated with DNS of decaying turbulence initialised by superimposing solenoidal velocity perturbations with a length scale of λ_f on isotropic turbulence. The number of vortices increases under the influence of perturbations with $\lambda_f/\eta \approx 30$, which promote the vortex formation from shear layers while the shear layers can survive for a longer time without the perturbations. The number

of vortices remains unchanged for perturbations with $\lambda_f/\eta \approx 70$. How the perturbations affect shear layer development is a small-scale process whose time scale is given by the Kolmogorov time scale. These results are consistent with numerical simulations of the isolated shear layer, where perturbations only with a certain wavelength can promote vortex formation. The amplitude of velocity perturbations u_f affects the increment in the number of vortices, which is more relevant to the ratio of u_f to u_η rather than that to u_{rms}. As u_η/u_{rms} decreases with a Reynolds number, less turbulent kinetic energy is required for the perturbations to cause an increase in the number of vortices at a higher Reynolds number. For the present DNS, the number of vortices increases by more than 10 % when u_f is $1.4u_\eta$. The shear layers are generated or sustained by energetic motions induced by the vortices (Watanabe & Nagata 2022). In addition, shear layer is split into more than one shear layer during the roll-up (Passot *et al.* 1995; Watanabe *et al.* 2020). Therefore, more shear layers appear in turbulence when the perturbations increase the number of vortices. The external perturbations which promote the shear instability also enhance the kinetic energy dissipation, enstrophy production and strain self-amplification because these are significantly enhanced by shearing motion.

DNS of decaying turbulence has also been carried out with an initial condition obtained by applying a band-cut filter to isotropic turbulence. When the velocity fluctuations with a wavelength of 30η are eliminated, the shear layers tend to persist for a long time, resulting in fewer vortices. The reduction in the number of vortices does not occur when the filter is applied to an energy-containing length scale. Thus, turbulent motions with a length of 30η play a dynamically important role in vortex formation by small-scale shear instability. Vortices frequently appear near and within shear layers (Horiuti & Takagi 2005; Elsinga & Marusic 2010; Watanabe & Nagata 2022; Nakamura *et al.* 2023). However, the filter that leads to the suppression of the shear instability does not affect these vortices. Therefore, rotating motions observed around the shear layers are not directly related to the velocity fluctuations which efficiently promote the shear instability.

The present study has confirmed that perturbations with the unstable wavelength of small-scale shear instability can efficiently modulate small-scale turbulent structures. The effects observed for the number of vortices can be important in many phenomena related to vortices in turbulence. One of the examples is turbulent entrainment in intermittent flows such as jets, mixing layers and boundary layers, where a turbulent/non-turbulent interface appears between turbulent and outer non-turbulent regions (da Silva *et al.* 2014). Previous studies of the interface have revealed that small-scale vortices near the interface are relevant to the local entrainment of non-turbulent fluids (Mathew & Basu 2002; Holzner & Lüthi 2011; Taveira & da Silva 2014; Watanabe *et al.* 2016, 2017*a*; Neamtu-Halic *et al.* 2021). The increase in the number of vortices by perturbations will be possibly important in the enhancement of entrainment by external disturbance. Further investigations are required for future applications of small-scale shear instability to turbulence modulation.

Acknowledgements. Numerical simulations presented in this paper were performed using the high-performance computing systems at the Japan Agency for Marine-Earth Science and Technology and Nagoya University. This work was also supported by Collaborative Research Project on Computer Science with High-Performance Computing in Nagoya University.

Funding. This work was supported by JSPS KAKENHI grant numbers 20H05754, 22K03903 and 22H01398.

Data availability statement. The data that support the findings of this study are available from the corresponding author upon reasonable request.

Declaration of interests. The authors report no conflict of interest.

Author ORCIDs.
Tomoaki Watanabe https://orcid.org/0000-0002-9375-0075;
Koji Nagata https://orcid.org/0000-0002-8519-5454.

References

Abraham, J. & Magi, V. 1997 Exploring velocity and density ratio effects in a mixing layer using DNS. *Intl J. Comput. Fluid Dyn.* **8** (2), 147–151.
Aluie, H. & Eyink, G.L. 2009 Localness of energy cascade in hydrodynamic turbulence. II. Sharp spectral filter. *Phys. Fluids* **21** (11), 115108.
Baerenzung, J., Mininni, P.D., Pouquet, A., Politano, H. & Ponty, Y. 2010 Spectral modeling of rotating turbulent flows. *Phys. Fluids* **22** (2), 025104.
Beronov, K.N. & Kida, S. 1996 Linear two-dimensional stability of a Burgers vortex layer. *Phys. Fluids* **8** (4), 1024–1035.
Betchov, R. & Szewczyk, A. 1963 Stability of a shear layer between parallel streams. *Phys. Fluids* **6** (10), 1391–1396.
Bhatt, K. & Tsuji, Y. 2021 Identification of vortex structures in flow fields using tomographic PIV method. *J. Fluid Sci. Tech.* **16** (3), JFST0018.
Brehm, C., Gross, A. & Fasel, H.F. 2013 Open-loop flow-control investigation for airfoils at low Reynolds numbers. *AIAA J.* **51** (8), 1843–1860.
Brown, G.L. & Roshko, A. 1974 On density effects and large structure in turbulent mixing layers. *J. Fluid Mech.* **64** (4), 775–816.
Buaria, D., Pumir, A., Bodenschatz, E. & Yeung, P.-K. 2019 Extreme velocity gradients in turbulent flows. *New J. Phys.* **21** (4), 043004.
Burgers, J.M. 1948 A mathematical model illustrating the theory of turbulence. *Adv. Appl. Mech.* **1**, 171–199.
Buxton, O.R.H. & Ganapathisubramani, B. 2010 Amplification of enstrophy in the far field of an axisymmetric turbulent jet. *J. Fluid Mech.* **651**, 483–502.
Buzzicotti, M., Biferale, L. & Toschi, F. 2020 Statistical properties of turbulence in the presence of a smart small-scale control. *Phys. Rev. Lett.* **124** (8), 084504.
Cao, N., Chen, S. & Doolen, G.D. 1999 Statistics and structures of pressure in isotropic turbulence. *Phys. Fluids* **11** (8), 2235–2250.
Carroll, P.L. & Blanquart, G. 2013 A proposed modification to Lundgren's physical space velocity forcing method for isotropic turbulence. *Phys. Fluids* **25** (10), 105114.
Caulfield, C.P. & Peltier, W.R. 1994 Three dimensionalization of the stratified mixing layer. *Phys. Fluids* **6** (12), 3803–3805.
Cazaubiel, A., Gorce, J.-B., Bacri, J.-C., Berhanu, M., Laroche, C. & Falcon, E. 2021 Three-dimensional turbulence generated homogeneously by magnetic particles. *Phys. Rev. Fluids* **6** (11), L112601.
Chen, X., Chung, Y.M. & Wan, M. 2021 The uniform-momentum zones and internal shear layers in turbulent pipe flows at Reynolds numbers up to $Re_\tau = 1000$. *Intl J. Heat Fluid Flow* **90**, 108817.
Chong, M.S., Perry, A.E. & Cantwell, B.J. 1990 A general classification of three-dimensional flow fields. *Phys. Fluids* **2** (5), 765–777.
Cimbala, J.M., Nagib, H.M. & Roshko, A. 1988 Large structure in the far wakes of two-dimensional bluff bodies. *J. Fluid Mech.* **190**, 265–298.
Corcos, G.M. & Lin, S.J. 1984 The mixing layer: deterministic models of a turbulent flow. Part 2. The origin of the three-dimensional motion. *J. Fluid Mech.* **139**, 67–95.
Crow, S.C. & Champagne, F.H. 1971 Orderly structure in jet turbulence. *J. Fluid Mech.* **48** (3), 547–591.
Das, R. & Girimaji, S.S. 2020 Characterization of velocity-gradient dynamics in incompressible turbulence using local streamline geometry. *J. Fluid Mech.* **895**, A5.
Davidson, P.A. 2004 *Turbulence: An Introduction for Scientists and Engineers*. Oxford University Press.
Doan, N.A.K., Swaminathan, N. & Chakraborty, N. 2017 Multiscale analysis of turbulence-flame interaction in premixed flames. *Proc. Combust. Inst.* **36** (2), 1929–1935.
Eisma, J., Westerweel, J., Ooms, G. & Elsinga, G.E. 2015 Interfaces and internal layers in a turbulent boundary layer. *Phys. Fluids* **27** (5), 055103.
Elsinga, G.E., Ishihara, T., Goudar, M.V., da Silva, C.B. & Hunt, J.C.R. 2017 The scaling of straining motions in homogeneous isotropic turbulence. *J. Fluid Mech.* **829**, 31–64.
Elsinga, G.E. & Marusic, I. 2010 Universal aspects of small-scale motions in turbulence. *J. Fluid Mech.* **662**, 514–539.

FAN, D., XU, J., YAO, M.X. & HICKEY, J.-P. 2019 On the detection of internal interfacial layers in turbulent flows. *J. Fluid Mech.* **872**, 198–217.

FISCALETTI, D., BUXTON, O.R.H. & ATTILI, A. 2021 Internal layers in turbulent free-shear flows. *Phys. Rev. Fluids* **6** (3), 034612.

GANAPATHISUBRAMANI, B., LAKSHMINARASIMHAN, K. & CLEMENS, N.T. 2008 Investigation of three-dimensional structure of fine scales in a turbulent jet by using cinematographic stereoscopic particle image velocimetry. *J. Fluid Mech.* **598**, 141–175.

GHIRA, A.A., ELSINGA, G.E. & DA SILVA, C.B. 2022 Characteristics of the intense vorticity structures in isotropic turbulence at high Reynolds numbers. *Phys. Rev. Fluids* **7** (10), 104605.

GHONIEM, A.F. & NG, K.K. 1987 Numerical study of the dynamics of a forced shear layer. *Phys. Fluids* **30** (3), 706–721.

GOTO, S., SAITO, Y. & KAWAHARA, G. 2017 Hierarchy of antiparallel vortex tubes in spatially periodic turbulence at high Reynolds numbers. *Phys. Rev. Fluids* **2** (6), 064603.

GOTO, S. & VASSILICOS, J.C. 2016 Unsteady turbulence cascades. *Phys. Rev.* E **94** (5), 053108.

GUL, M., ELSINGA, G.E. & WESTERWEEL, J. 2020 Internal shear layers and edges of uniform momentum zones in a turbulent pipe flow. *J. Fluid Mech.* **901**, A10.

GUTMARK, E.J., SCHADOW, K.C. & YU, K.H. 1995 Mixing enhancement in supersonic free shear flows. *Annu. Rev. Fluid Mech.* **27** (1), 375–417.

HAYASHI, M., WATANABE, T. & NAGATA, K. 2021*a* Characteristics of small-scale shear layers in a temporally evolving turbulent planar jet. *J. Fluid Mech.* **920**, A38.

HAYASHI, M., WATANABE, T. & NAGATA, K. 2021*b* The relation between shearing motions and the turbulent/non-turbulent interface in a turbulent planar jet. *Phys. Fluids* **33** (5), 055126.

HIROTA, M., NISHIO, Y., IZAWA, S. & FUKUNISHI, Y. 2017 Vortex stretching in a homogeneous isotropic turbulence. In *J. Phys.: Conf. Ser.*, vol. 822, 012041. IOP.

HOLZNER, M. & LÜTHI, B. 2011 Laminar superlayer at the turbulence boundary. *Phys. Rev. Lett.* **106** (13), 134503.

HORIUTI, K. & TAKAGI, Y. 2005 Identification method for vortex sheet structures in turbulent flows. *Phys. Fluids* **17** (12), 121703.

JAHANBAKHSHI, R., VAGHEFI, N.S. & MADNIA, C.K. 2015 Baroclinic vorticity generation near the turbulent/non-turbulent interface in a compressible shear layer. *Phys. Fluids* **27** (10), 105105.

JEONG, J. & HUSSAIN, F. 1995 On the identification of a vortex. *J. Fluid Mech.* **285**, 69–94.

JIMÉNEZ, J. 2018 Machine-aided turbulence theory. *J. Fluid Mech.* **854**, R1.

JIMÉNEZ, J. & MOIN, P. 1991 The minimal flow unit in near-wall turbulence. *J. Fluid Mech.* **225**, 213–240.

JIMÉNEZ, J. & WRAY, A.A. 1998 On the characteristics of vortex filaments in isotropic turbulence. *J. Fluid Mech.* **373**, 255–285.

JIMÉNEZ, J., WRAY, A.A., SAFFMAN, P.G. & ROGALLO, R.S. 1993 The structure of intense vorticity in isotropic turbulence. *J. Fluid Mech.* **255**, 65–90.

JOHNSEN, E., *et al.* 2010 Assessment of high-resolution methods for numerical simulations of compressible turbulence with shock waves. *J. Comput. Phys.* **229** (4), 1213–1237.

KANG, S.-J., TANAHASHI, M. & MIYAUCHI, T. 2007 Dynamics of fine scale eddy clusters in turbulent channel flows. *J. Turbul.* **8**, N52.

KATAGIRI, T., WATANABE, T. & NAGATA, K. 2021 Statistical properties of a model of a turbulent patch arising from a breaking internal wave. *Phys. Fluids* **33** (5), 055107.

KHOLMYANSKY, M., TSINOBER, A. & YORISH, S. 2001 Velocity derivatives in the atmospheric surface layer at $Re_\lambda = 10^4$. *Phys. Fluids* **13** (1), 311–314.

KIDA, S. & MIURA, H. 1998 Identification and analysis of vortical structures. *Eur. J. Mech. (*B*/Fluids)* **17** (4), 471–488.

KOLÁŘ, V. 2007 Vortex identification: new requirements and limitations. *Intl J. Heat Fluid Flow* **28** (4), 638–652.

KOLÁŘ, V. & ŠÍSTEK, J. 2014 Recent progress in explicit shear-eliminating vortex identification. In *Proceedings of the 19th Australasian Fluid Mechanics Conference*. Australasian Fluid Mechanics Society Australia.

KOLMOGOROV, A.N. 1941 Local structure of turbulence in an incompressible fluid for very large Reynolds numbers. *Dokl. Akad. Nauk SSSR* **30**, 299–303.

LE RIBAULT, C., SARKAR, S. & STANLEY, S.A. 1999 Large eddy simulation of a plane jet. *Phys. Fluids* **11** (10), 3069–3083.

LEUNG, T., SWAMINATHAN, N. & DAVIDSON, P.A. 2012 Geometry and interaction of structures in homogeneous isotropic turbulence. *J. Fluid Mech.* **710**, 453–481.

LIN, S.J. & CORCOS, G.M. 1984 The mixing layer: deterministic models of a turbulent flow. Part 3. The effect of plane strain on the dynamics of streamwise vortices. *J. Fluid Mech.* **141**, 139–178.
LIU, C., GAO, Y., TIAN, S. & DONG, X. 2018 Rortex-a new vortex vector definition and vorticity tensor and vector decompositions. *Phys. Fluids* **30** (3), 035103.
MASLOWE, S.A. & THOMPSON, J.M. 1971 Stability of a stratified free shear layer. *Phys. Fluids* **14** (3), 453–458.
MATHEW, J. & BASU, A.J. 2002 Some characteristics of entrainment at a cylindrical turbulence boundary. *Phys. Fluids* **14** (7), 2065–2072.
MAXEY, M. 2017 Simulation methods for particulate flows and concentrated suspensions. *Annu. Rev. Fluid Mech.* **49**, 171–193.
MILES, J.W. 1961 On the stability of heterogeneous shear flows. *J. Fluid Mech.* **10** (4), 496–508.
MONIN, A.S. & YAGLOM, A.M. 1975 *Statistical Fluid Mechanics*, vol. 2. MIT Press.
MORINISHI, Y., LUND, T.S., VASILYEV, O.V. & MOIN, P. 1998 Fully conservative higher order finite difference schemes for incompressible flow. *J. Comput. Phys.* **143** (1), 90–124.
MOSER, R.D. & ROGERS, M.M. 1991 Mixing transition and the cascade to small scales in a plane mixing layer. *Phys. Fluids* **3** (5), 1128–1134.
MOURI, H., HORI, A. & KAWASHIMA, Y. 2007 Laboratory experiments for intense vortical structures in turbulence velocity fields. *Phys. Fluids* **19** (5), 055101.
NAGATA, R., WATANABE, T., NAGATA, K. & DA SILVA, C.B. 2020 Triple decomposition of velocity gradient tensor in homogeneous isotropic turbulence. *Comput. Fluids* **198**, 104389.
NAKAMURA, K., WATANABE, T. & NAGATA, K. 2023 Turbulent/turbulent interfacial layers of a shearless turbulence mixing layer in temporally evolving grid turbulence. *Phys. Fluids* **35** (4), 045117.
NEAMTU-HALIC, M.M., MOLLICONE, J.-P., VAN REEUWIJK, M. & HOLZNER, M. 2021 Role of vortical structures for enstrophy and scalar transport in flows with and without stable stratification. *J. Turbul.* **22** (7), 393–412.
OHKITANI, K. & KIDA, S. 1992 Triad interactions in a forced turbulence. *Phys. Fluids* **4** (4), 794–802.
OKONG'O, N.A. & BELLAN, J. 2002 Direct numerical simulation of a transitional supercritical binary mixing layer: heptane and nitrogen. *J. Fluid Mech.* **464**, 1–34.
OSTER, D. & WYGNANSKI, I. 1982 The forced mixing layer between parallel streams. *J. Fluid Mech.* **123**, 91–130.
PASSOT, T., POLITANO, H., SULEM, P.L., ANGILELLA, J.R. & MENEGUZZI, M. 1995 Instability of strained vortex layers and vortex tube formation in homogeneous turbulence. *J. Fluid Mech.* **282**, 313–338.
PATNAIK, P.C., SHERMAN, F.S. & CORCOS, G.M. 1976 A numerical simulation of Kelvin–Helmholtz waves of finite amplitude. *J. Fluid Mech.* **73** (2), 215–240.
PHILIP, J. & MARUSIC, I. 2012 Large-scale eddies and their role in entrainment in turbulent jets and wakes. *Phys. Fluids* **24** (5), 055108.
PIROZZOLI, S., BERNARDINI, M. & GRASSO, F. 2010 On the dynamical relevance of coherent vortical structures in turbulent boundary layers. *J. Fluid Mech.* **648**, 325–349.
POPE, S.B. 2000 *Turbulent Flows*. Cambridge University Press.
ROSALES, C. & MENEVEAU, C. 2005 Linear forcing in numerical simulations of isotropic turbulence: physical space implementations and convergence properties. *Phys. Fluids* **17** (9), 095106.
SAMIMY, M., WEBB, N. & CRAWLEY, M. 2018 Excitation of free shear-layer instabilities for high-speed flow control. *AIAA J.* **56** (5), 1770–1791.
SIGGIA, E.D. 1981 Numerical study of small-scale intermittency in three-dimensional turbulence. *J. Fluid Mech.* **107**, 375–406.
DA SILVA, C.B., DOS REIS, R.J.N. & PEREIRA, J.C.F. 2011 The intense vorticity structures near the turbulent/non-turbulent interface in a jet. *J. Fluid Mech.* **685**, 165–190.
DA SILVA, C.B., HUNT, J.C.R., EAMES, I. & WESTERWEEL, J. 2014 Interfacial layers between regions of different turbulence intensity. *Annu. Rev. Fluid Mech.* **46**, 567–590.
ŠÍSTEK, J., KOLÁŘ, V., CIRAK, F. & MOSES, P. 2012 Fluid–structure interaction and vortex identification. In *Proceedings of the 18th Australasian Fluid Mechanics Conference*. Australasian Fluid Mechanics Society Australia.
SOTERIOU, M.C. & GHONIEM, A.F. 1995 Effects of the free-stream density ratio on free and forced spatially developing shear layers. *Phys. Fluids* **7** (8), 2036–2051.
SPALART, P.R., MOSER, R.D. & ROGERS, M.M. 1991 Spectral methods for the Navier–Stokes equations with one infinite and two periodic directions. *J. Comput. Phys.* **96** (2), 297–324.
SREENIVASAN, K.R. & ANTONIA, R.A. 1997 The phenomenology of small-scale turbulence. *Annu. Rev. Fluid Mech.* **29** (1), 435–472.

STANLEY, S.A., SARKAR, S. & MELLADO, J.P. 2002 A study of the flow-field evolution and mixing in a planar turbulent jet using direct numerical simulation. *J. Fluid Mech.* **450**, 377–407.

TAKAMURE, K., SAKAI, Y., ITO, Y., IWANO, K. & HAYASE, T. 2019 Dissipation scaling in the transition region of turbulent mixing layer. *Intl J. Heat Fluid Flow* **75**, 77–85.

TANAHASHI, M., IWASE, S. & MIYAUCHI, T. 2001 Appearance and alignment with strain rate of coherent fine scale eddies in turbulent mixing layer. *J. Turbul.* **2** (6), 1–18.

TAVEIRA, R.R. & DA SILVA, C.B. 2014 Characteristics of the viscous superlayer in shear free turbulence and in planar turbulent jets. *Phys. Fluids* **26** (2), 021702.

TSINOBER, A. 2009 *An Informal Conceptual Introduction to Turbulence*. Springer.

VINCENT, A. & MENEGUZZI, M. 1994 The dynamics of vorticity tubes in homogeneous turbulence. *J. Fluid Mech.* **258**, 245–254.

VREMAN, B., GEURTS, B. & KUERTEN, H. 1995 A priori tests of large eddy simulation of the compressible plane mixing layer. *J. Engng Maths* **29** (4), 299–327.

WATANABE, T., JAULINO, R., TAVEIRA, R.R., DA SILVA, C.B., NAGATA, K. & SAKAI, Y. 2017*a* Role of an isolated eddy near the turbulent/non-turbulent interface layer. *Phys. Rev. Fluids* **2** (9), 094607.

WATANABE, T. & NAGATA, K. 2018 Integral invariants and decay of temporally developing grid turbulence. *Phys. Fluids* **30** (10), 105111.

WATANABE, T. & NAGATA, K. 2022 Energetics and vortex structures near small-scale shear layers in turbulence. *Phys. Fluids* **34** (9), 095114.

WATANABE, T., RILEY, J.J., NAGATA, K., ONISHI, R. & MATSUDA, K. 2018 A localized turbulent mixing layer in a uniformly stratified environment. *J. Fluid Mech.* **849**, 245–276.

WATANABE, T., DA SILVA, C.B., NAGATA, K. & SAKAI, Y. 2017*b* Geometrical aspects of turbulent/non-turbulent interfaces with and without mean shear. *Phys. Fluids* **29** (8), 085105.

WATANABE, T., DA SILVA, C.B., SAKAI, Y., NAGATA, K. & HAYASE, T. 2016 Lagrangian properties of the entrainment across turbulent/non-turbulent interface layers. *Phys. Fluids* **28** (3), 031701.

WATANABE, T., TANAKA, K. & NAGATA, K. 2020 Characteristics of shearing motions in incompressible isotropic turbulence. *Phys. Rev. Fluids* **5** (7), 072601.

WATANABE, T., TANAKA, K. & NAGATA, K. 2021 Solenoidal linear forcing for compressible, statistically steady, homogeneous isotropic turbulence with reduced turbulent mach number oscillation. *Phys. Fluids* **33** (9), 095108.

WATANABE, T., ZHANG, X. & NAGATA, K. 2019 Direct numerical simulation of incompressible turbulent boundary layers and planar jets at high Reynolds numbers initialized with implicit large eddy simulation. *Comput. Fluids* **194**, 104314.

WATANABE, T., ZHENG, Y. & NAGATA, K. 2022 The decay of stably stratified grid turbulence in a viscosity-affected stratified flow regime. *J. Fluid Mech.* **946**, A29.

YEUNG, P.K. & BRASSEUR, J.G. 1991 The response of isotropic turbulence to isotropic and anisotropic forcing at the large scales. *Phys. Fluids* **3** (5), 884–897.

YULE, A.J. 1978 Large-scale structure in the mixing layer of a round jet. *J. Fluid Mech.* **89** (3), 413–432.